

Energetics and Kinetics of Primary Charge Separation in Bacterial Photosynthesis

David N. LeBard, Vitaliy Kapko, and Dmitry V. Matyushov*

Center for Biological Physics, Arizona State University, P.O. Box 871604, Tempe, Arizona 85287-1604

Received: February 25, 2008; Revised Manuscript Received: May 7, 2008

We report the results of molecular dynamics (MD) simulations and formal modeling of the free-energy surfaces and reaction rates of primary charge separation in the reaction center of *Rhodobacter sphaeroides*. Two simulation protocols were used to produce MD trajectories. Standard force-field potentials were employed in the first protocol. In the second protocol, the special pair was made polarizable to reproduce a high polarizability of its photoexcited state observed by Stark spectroscopy. The charge distribution between covalent and charge-transfer states of the special pair was dynamically adjusted during the simulation run. We found from both protocols that the breadth of electrostatic fluctuations of the protein/water environment far exceeds previous estimates, resulting in about 1.6 eV reorganization energy of electron transfer in the first protocol and 2.5 eV in the second protocol. Most of these electrostatic fluctuations become dynamically frozen on the time scale of primary charge separation, resulting in much smaller solvation contributions to the activation barrier. While water dominates solvation thermodynamics on long observation times, protein emerges as the major thermal bath coupled to electron transfer on the picosecond time of the reaction. Marcus parabolas were obtained for the free-energy surfaces of electron transfer by using the first protocol, while a highly asymmetric surface was obtained in the second protocol. A nonergodic formulation of the diffusion-reaction electron-transfer kinetics has allowed us to reproduce the experimental results for both the temperature dependence of the rate and the nonexponential decay of the population of the photoexcited special pair.

I. Introduction

The problem of bacterial photosynthesis has received enormous attention from both experimental and theoretical communities.^{1–6} Here, we consider only the first step in the sequence of electronic transitions following the absorption of a visible photon by the special pair of the reaction center, the primary charge separation. The calculation of the rate of primary charge separation, which over several decades of intense research has effectively become the hydrogen molecule of bioenergetics, involves two components: the electronic communication between the primary donor and acceptor responsible for electron tunneling^{7–9} and the Franck–Condon factor describing the probability of bringing the donor and acceptor levels into resonance with each other.^{10,11} Our paper is concerned with that latter part of the problem which we dub as the energetics of primary charge separation.^{12–14}

In addressing the issue of the energetics of charge separation, we first want to dissect this complex problem into two, not necessarily simpler, questions: (1) What is the importance of the structural arrangement of the cofactors in the reaction center protein? (2) What are the roles played by the protein and hydrating water in activating electronic transitions? Each of these questions has generated a significant amount of literature on its own, and we will not be able to provide a comprehensive discussion of each topic, focusing instead on our main goal, the factors affecting the free energy of activation.

Since optical spectroscopy of bacteriochlorophyll cofactors can be studied separately, the most intriguing question related to our discussion is how the energetics of optical transitions and electron transfer are affected when the cofactors are assembled within the protein matrix. The notion often circulated in the literature⁵ is that protein provides a low-polarity environment, lowering the free energy of solvation of embedded cofactors compared to solvation in water. Even though this

statement is generally correct, we will show below that nuclear solvation approaching the thermodynamic limit of infinite observation (waiting) time is still quite significant for the electron-transfer dipole formed by difference occupation numbers (atomic charges) of the electron in the donor and acceptor states. In particular, solvation of the electron-transfer dipole by water is not fully screened by the protein and still makes about 1 eV. In addition, the protein matrix cannot be really considered nonpolar, since there is a significant contribution to the reorganization energy from the nuclear modes of the protein. It turns out that the notion of weak nuclear solvation of primary charge separation, required to explain the observed rates, cannot fully rest on the thermodynamic arguments, and the dynamics of the protein/water thermal bath need to be involved.

Solvation dynamics of optical chromophores in dense molecular solvents have been actively studied in the past decades.^{15–17} The basic picture, first discovered in numerical simulations¹⁸ and later confirmed by laboratory measurements,¹⁶ is that the decay of the solvation correlation function (Stokes shift correlation function, $S(t)$) involves two major components. The fast Gaussian component is caused by ballistic motions of the solvent in the first solvation shell of the solute (quasi-localized vibrations in the case of a protein). The slow tail of $S(t)$ is related to collective α relaxation mostly caused by relaxation of orientations of molecular permanent dipoles (dielectric relaxation) and quadrupoles.¹⁷ The notion of α relaxation, that is, the slowest relaxation on the microscopic scale, is not commonly invoked in the discussion of high-temperature solvation dynamics of small molecular dyes¹⁹ but becomes critical in building a conceptual basis for understanding the solvation dynamics of cofactors assembled within the hydrated protein.²⁰

Phenomenology developed for structural glass-formers²¹ helps to formulate the problem we are dealing with here. The typical temperature dependence of the relaxation time of a polar

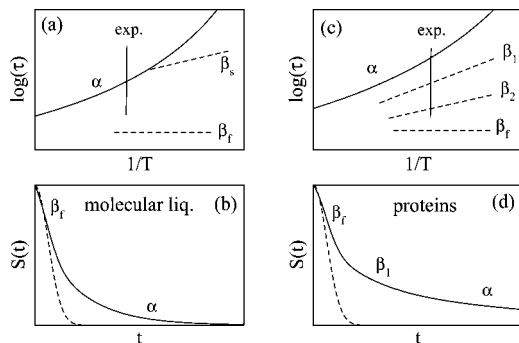


Figure 1. Relaxation times (a, c) and the Stokes shift dynamics (b, d) of the structural glass-formers (a, b) and proteins (c, d). The vertical lines marked “exp.” denote the temperature at which the Stokes shift correlation function is recorded. The dashed lines in parts b and d show the fast Gaussian decay of $S(t)$.

molecular liquid is shown in Figure 1a. A high-temperature liquid has two relaxation times: reorientations of molecular permanent dipoles resulting in slow α relaxation and fast β_f relaxation related to collective anharmonic cage rattling. Correspondingly, the Stokes shift correlation function has two components: fast Gaussian decay coupled to β_f molecular motions and a slow tail coupled to α motions. This latter component is often connected to dielectric relaxation of the homogeneous solvent.²² When the liquid is supercooled, the α component, which often becomes non-Arrhenius, separates from the slow β relaxation (β_s) characterized by the Arrhenius temperature dependence²¹ (Figure 1a). If all the components of the Stokes shift correlation function could be resolved at that low temperature, three major parts, corresponding to α , β_s , and β_f relaxation, could have been seen. It is this imaginary experiment, which is hard to realize in molecular liquids,²³ that bears a close connection to charge-transfer dynamics in proteins.

For proteins, as well as for most polymer glass-formers, α and β relaxation are well separated in the temperature range of protein stability.^{20,24,25} In addition, the secondary β relaxation is typically split into several components with increasingly faster dynamics accompanied by smaller activation barriers (Figure 1c). The rugged surface of the protein also complicates the dynamics, and α relaxation is known to disappear from the response of water in nanoconfinement.²⁶ The coupling of the transferred electron to different modes of the protein/water solvent may vary, and it is *a priori* not clear which mode will dominate the solvation dynamics. However, one can clearly expect Stokes shift dynamics to show at least three components including a Gaussian decay due to β_f modes, some subset of β_s modes, and an α relaxation (Figure 1d). The relative relaxation times and weights of these modes in the overall Stokes shift correlation function are critical for the energetics of charge transfer, as we show below.

The geometric arrangement of cofactors in the membrane protein of the reaction center has been considered in the literature mostly from the perspective of calculating the probability of electron tunneling incorporated into the electron-transfer matrix element.⁷ Early studies considered the possibility of direct charge separation from the special pair (P) to bacteriopheophytin (H_L) of the L-branch of monomeric chromophores via a superexchange mechanism involving nearby bacteriochlorophyll (B_L).^{10,27} More recent studies^{12,28–31} have identified B_L^- as an intermediate state in the sequence of electron hops,³² a slower process from P^* to B_L followed by a faster transition from B_L to H_L . The energy level of B_L^- was placed between 331–450 cm^{-1} (refs 28 and 30) and 650–800 cm^{-1} (ref 33) below the energy level

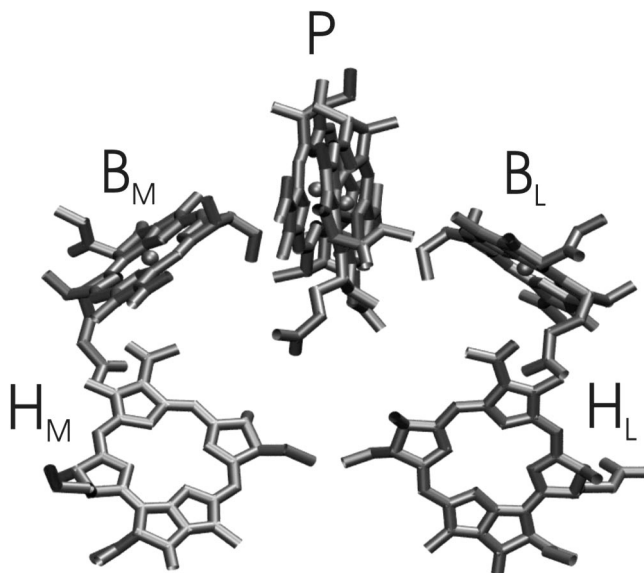


Figure 2. Schematic arrangement of cofactors in the bacterial reaction center. P is the special pair, and B and H are monomeric bacteriochlorophylls and bacteriopheophytins, respectively. Electron transfer in wild-type reaction centers occurs almost exclusively along the L-branch of cofactors (subscript “L”), while the M-branch (subscript “M”) is mostly inactive.

of the excited special pair P^* , favoring in both cases sequential over superexchange transfer. In the present study, we will restrict our attention to the first of two hops, limiting our calculations to the rate of transition from P^* to B_L (Figure 2).

The role of the structural arrangement of the special pair in the energetics of primary charge separation has attracted relatively little attention (see, however, Warshel’s work³⁴). The spectroscopy of the $P \rightarrow P^*$ excitation and of the special pair cation radical has been intensely studied,^{35,36} along with extensive modeling of the energy transfer within the antenna complex and to the special pair.³⁷ The question we address here is somewhat different. Given that the special pair has evolved within the reaction center, we wonder if its particular structural arrangement makes any significant impact on the activation barrier of primary charge separation. Since the sandwich of two bacteriochlorophylls making P is highly conserved in bacterial and plant photosynthesis,⁵ it might have some other role in the functionality of the reaction center aside from capturing the excitation from the antenna complex.

The motivation for posing this question is provided by Stark experiments by Boxer and co-workers who showed a dramatic increase of the polarizability of P upon photoexcitation.³⁸ In fact, the polarizability change of about 10^3 \AA^3 upon photoexcitation³⁸ places the special pair among the most polarizable molecules known (carotenoids, also present in the reaction center, make another group of champions). This remarkable observation is combined here with our previous studies of electron transfer in polarizable donor–acceptor complexes,^{39–41} which showed that the change in polarizability accompanying charge-transfer results in asymmetric, nonparabolic free-energy surfaces for electron transfer. Determining whether this polarization asymmetry can significantly affect the activation barrier is one of the goals of this study.

In summary, by combining extensive molecular dynamics (MD) simulations with formal modeling, we want to establish the basic ingredients contributing to the activation barrier of primary charge separation. The questions we address are the following: (1) What is the set of primary nuclear modes (either

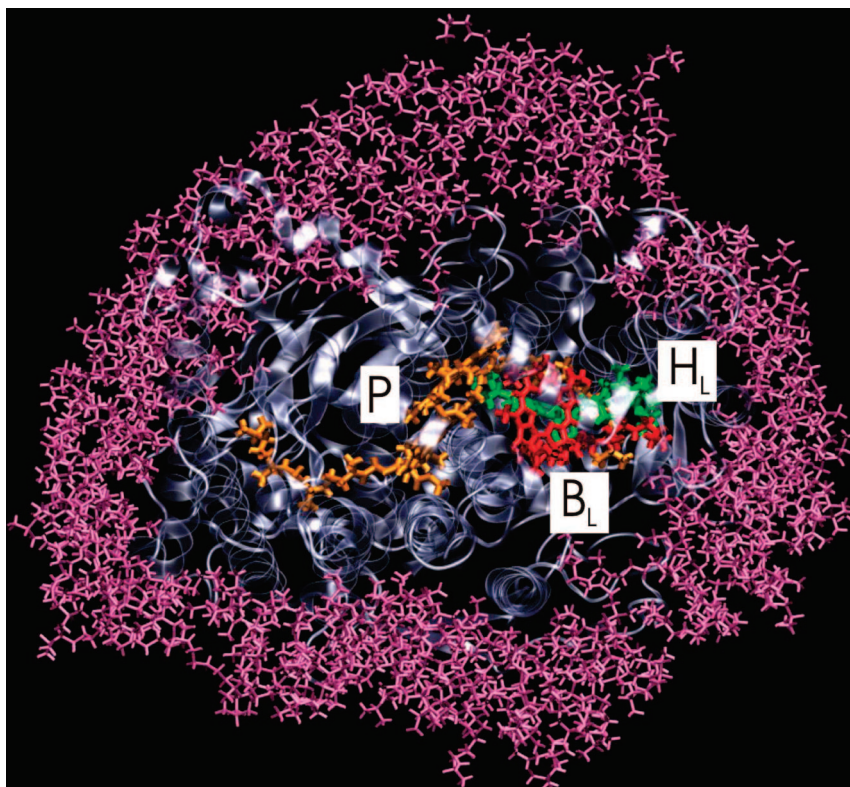


Figure 3. Reaction complex of *Rhodobacter sphaeroides*.⁴² The protein (gray) is surrounded by the micelle of LDAO detergent molecules (purple). The electron is transferred in sequence from the photoexcited special pair (P, gold) to bacteriochlorophyll (B_L , red) followed by even faster transfer to bacteriopheophytin (H_L , green). In MD simulations, the reaction complex is surrounded by 6 sodium ions, 30 NaCl pairs, and 10 506 water molecules which are not shown here.

protein or aqueous water/protein interface) that promote transfer of an electron? (2) How to describe the activation events happening on such a short reaction time? In particular, we show that nonergodic chemical kinetics is required in this case to replace the standard Marcus picture based on equilibrium distributions. (3) What is the effect of high polarizability of the photoinduced special pair on the energetics of the transition?

We address the questions posed above by incorporating the Stokes shift dynamics from MD simulations into a formal theory which we describe first below. The results of the calculations presented next are tested for consistency against experimental data. We use our simulation data obtained at different temperatures to compare the calculated rates with the results of Fleming et al.¹ In addition, the recently published data by Wang et al.⁴³ for the population decay of the photoexcited state of the special pair in a number of mutants offer an opportunity to use the dynamical electron-transfer models^{44–46} to study the multiexponential population decay. These experimental results are also analyzed here by combining the Stokes shift dynamics from MD simulations with a formal model of nonergodic chemical kinetics. The picture that has emerged from all this effort is summarized in the Discussion section of this paper.

II. Basics of the Formalism

We approach the problem of calculating the rates of charge separation by combining the input from MD simulations with analytical formalism. Simulations of the reaction center of *Rhodobacter sphaeroides*⁴² were carried out using Amber 8.0.⁴⁷ We have followed the procedure first suggested by Ceccarelli and Marchi^{48,49} in which the reaction center is surrounded by the micelle of detergent (lauryl dimethyl amino oxide, LDAO) molecules mimicking the hydrophobic membrane, and also

closely matching the experimental setup⁵⁰ for photochemical studies of bacterial photosynthesis. The structure of the reaction center surrounded by LDAO molecules is shown in Figure 3. The details of the simulation protocol are provided in Appendix A, and the charging scheme of the cofactors and the protein/water solvent is outlined in Appendix B.

A. Energetics of Primary Charge Separation. Electron transfer is a tunneling event realized, in the Born–Oppenheimer approximation, at the resonance of the electronic donor and acceptor energies. The gap between the electronic energies of the donor and acceptor states, ΔE , makes the one-dimensional reaction coordinate $X = \Delta E$ that incorporates the whole manifold of possible nuclear modes affecting the electronic transition.⁵¹ Because many nuclear motions affect the donor and acceptor states in dense condensed media, the fluctuations of the stochastic variable ΔE are often well represented by the Gaussian statistics.⁵² Therefore, the probability of reaching zero energy gap $\Delta E = 0$, when electron tunneling takes place, is given by the Gaussian function

$$P(\Delta E=0) \propto e^{-\langle \Delta E \rangle^2 / 2C_X(0)} \quad (1)$$

Here, the variance $C_X(0) = \langle (\delta X)^2 \rangle$, $\delta X = \Delta E - \langle \Delta E \rangle$, is equal to the $t = 0$ value of the time self-correlation function of the energy gap $X(t) = \Delta E(t)$

$$C_X(t) = \langle \delta X(t) \delta X(0) \rangle \quad (2)$$

and the brackets stand for an ensemble average.

If one multiplies the probability of reaching the resonance with the frequency ω_e of electron tunneling between the donor and acceptor electronic levels, one arrives at the Marcus–Levich equation for the electron-transfer rate⁵³

$$k_{\text{ET}} = \omega_e e^{-\langle \Delta E \rangle^2 / 2C_X(0)} \quad (3)$$

In the case of nonadiabatic electron transfer considered here (weak electronic coupling between the donor and acceptor), the electronic “tunneling frequency” is given in terms of the electron-transfer matrix element V by the following equation:

$$\omega_e = \sqrt{2\pi/C_X(0)}(V^2/\hbar) \quad (4)$$

Equation 3 is quite general and is limited only by the assumption of Gaussian fluctuations of the energy gap. In order to make it practical, one needs to connect the average energy gap $\langle \Delta E \rangle$ and the variance $C_X(0)$ to physical interactions present in the system made of the donor–acceptor complex and a thermal bath of nuclear degrees of freedom coupled to the transferred electron. Despite the obvious complexity of the system, a generally applicable separation of the average energy gap into three components is possible: the gas-phase gap ΔE^{gas} , the shift by nonpolar interaction potentials ΔE^{ind} , and the shift by Coulomb interactions between the permanent partial charges of the solute and the solvent, ΔE^{C} .

$$\langle \Delta E \rangle = \Delta E^{\text{gas}} + \Delta E^{\text{ind}} + \Delta E^{\text{C}} \quad (5)$$

The gas-phase energy gap ΔE^{gas} is the difference between the ionization potential of the donor and the electron affinity of the acceptor in the gas phase. The two other components represent ensemble averages of the interaction potential between the cofactors and the protein/water solvent. They can be combined into a solvent-induced (subscript “s”) average shift

$$\Delta E_s = \Delta E^{\text{ind}} + \Delta E^{\text{C}} \quad (6)$$

The separation of the solvent part of the average energy gap into nonpolar and Coulomb parts is in fact related to the separation of time scales first discussed in early work on polarons in solids by Pekar,^{54,55} Fröhlich,⁵⁶ and Feynman.⁵⁷ The fast electronic degrees of the solvent (which is composed of protein, detergent, and water in our problem) result in instantaneous equilibration of the transferred electron by induction and dispersion (London) forces. For our present application, the former is more significant (superscript “ind” in eq 5 and throughout below) and we therefore explicitly consider this component. The last term in eq 5, related to Coulomb interactions, fluctuates due to slow molecular motions of molecular rotations and translations. This term is often described in the electron-transfer literature by the coupling of the electric field of the donor–acceptor complex to the inertial dipolar polarization,⁵⁵ which we consider after the induction component.

The induction forces are produced by polarizing the medium by the electric field of the donor–acceptor complex. If atoms and/or molecules of the medium carry polarizabilities α_j , the induction energy is the sum of polarization free energies of all such polarizable groups located at positions r_j . The induction shift of the average energy gap is then given by the change in the polarization free energy caused by changing the electric field of the donor–acceptor complex

$$\Delta E^{\text{ind}} = - \left\langle \sum_j (\alpha_j/2) [E_{02}^2(\mathbf{r}_j) - E_{01}^2(\mathbf{r}_j)] \right\rangle \quad (7)$$

This component of the energy gap is often not given adequate attention in the electron-transfer literature, even though it can be quite significant,^{58,59} as we show below. The induction shift also depends on temperature for constant-pressure experiments because of thermal expansion, and this fact needs to be included in the modeling of temperature-dependent reaction rates. Even though the induction potential is established instantaneously by

induced electronic dipoles, the interaction energy is modulated by nuclear motions of the solvent (water and protein), producing a nonzero component in the Gaussian distribution width (see below).

The Coulomb part of the donor–acceptor energy gap has received the most attention over several decades of the theory development, and we will briefly set up the stage for our treatment of this part of the problem here. The linear response approximation, either in terms of the electrostatic interaction with the medium dipolar polarization⁶⁰ or in terms of partial atomic charges,⁶¹ has mostly been used as the basis for the theory development. In the former case, one considers the polarization of the solvent by the electric field of the solute \mathbf{E}_{01} in the initial electron-transfer state. This equilibrium polarization $\mathbf{P}_{\text{eq}}(\mathbf{r})$ at point \mathbf{r} within the solvent is connected to the field $\mathbf{E}_{01}(\mathbf{r}')$ at point \mathbf{r}' by generally a nonlocal response function $\chi(\mathbf{r}, \mathbf{r}')$ ^{61–63}

$$\mathbf{P}_{\text{eq}}(\mathbf{r}) = \chi(\mathbf{r}, \mathbf{r}') * \mathbf{E}_{01}(\mathbf{r}') \quad (8)$$

where the asterisk denotes volume integration over the variable \mathbf{r}' and tensor contraction over the Cartesian components of the field with the corresponding components of the 2-rank tensor χ .

Equation 8 for the solvent polarization induced by the solute typically appears in theories of linear solvation in homogeneous liquids. In contrast, the protein matrix itself and the protein/water interface are inhomogeneous with a possibility of generating a polarization field \mathbf{P}'_{eq} unrelated to the electric field of the cofactors. This polarization will create an additional inhomogeneous component of the vertical shift $\Delta E_{\text{inh}}^{\text{C}}$ that cannot be calculated from the linear response approximation. The inertial (nuclear) polarization field $\mathbf{P}'_{\text{eq}} + \mathbf{P}_{\text{eq}}$ does not change on the time scale of electronic transition and creates a shift of the donor–acceptor energy gap by the amount determined by the change in the electron’s electric field $\Delta \mathbf{E}_0$ upon the transition:

$$\Delta E^{\text{C}} = -(\mathbf{P}'_{\text{eq}} + \mathbf{P}_{\text{eq}}) * \Delta \mathbf{E}_0 = \Delta E_{\text{inh}}^{\text{C}} - \mathbf{E}_{01} * \chi * \Delta \mathbf{E}_0 \quad (9)$$

In the original Marcus formulation,⁵³ the average vertical energy gap was separated into the Coulomb reorganization energy λ^{C} and the Coulomb part of the Gibbs energy of the reaction, ΔG^{C} . By using the identity $\mathbf{E}_{01} = \bar{\mathbf{E}}_0 - \Delta \mathbf{E}_0/2$, $\bar{\mathbf{E}}_0 = (\mathbf{E}_{01} + \mathbf{E}_{02})/2$ in eq 9, one gets

$$\Delta E^{\text{C}} = \lambda^{\text{C}} + \Delta G^{\text{C}} \quad (10)$$

where

$$\lambda^{\text{C}} = (1/2) \Delta \mathbf{E}_0 * \chi * \Delta \mathbf{E}_0 \quad (11)$$

and

$$\Delta G^{\text{C}} = \Delta E_{\text{inh}}^{\text{C}} - \bar{\mathbf{E}}_0 * \chi * \Delta \mathbf{E}_0 \quad (12)$$

The Coulomb part of the Gibbs energy then combines with the gas-phase gap and the induction shift to make the overall reaction Gibbs energy

$$\Delta G = \Delta E^{\text{gas}} + \Delta E^{\text{ind}} + \Delta G^{\text{C}} \quad (13)$$

Combined together, eqs 5, 10, and 13 lead to the standard Marcus relation for the vertical average energy gap

$$\langle \Delta E \rangle = \Delta G + \lambda^{\text{C}} \quad (14)$$

The separation of the average energy gap into the equilibrium Gibbs energy and reorganization energy components makes sense when the former can be measured separately. In spectroscopy, the average gap is given by the maximum of the

corresponding spectroscopic band (or, more precisely, by the first spectral moment) and this separation is not necessary. Likewise, the average energy gap is directly accessible from MD simulations, so the formulation in terms of the average energy gap is also more convenient from the simulation perspective. Even more importantly, the Gibbs energy of the reaction loses its direct connection to equilibrium thermodynamics in nonergodic reaction kinetics, which we formulate and apply to the calculation of the rates below. In this framework, the formulation of electron-transfer energetics in terms of the first and second cumulants of the donor–acceptor energy gap is the only formal approach to the problem available at the moment.

The Gaussian width, $C_X(0)$ in eq 3, generally needs a separate determination. It is calculated as the variance of the sum of all solute–solvent interaction potentials affecting the energy of the transferred electron. The problem is simplified for the Coulomb interactions. These are long-ranged and are typically well described by the linear response approximation. Therefore, the high-temperature limit of the fluctuation dissipation theorem⁶⁴ applies to the Coulomb part on nuclear fluctuations with the resulting factorization of $C_X(0)$ into temperature and reorganization energy^{53,65}

$$C_X(0) = 2k_B T \lambda_s \quad (15)$$

A significant simplification of this route is achieved through the fact that the variance is determined in terms of the same response function as the one used for the Coulomb part of the average energy gap (eq 9), thus reducing the number of independent response functions required by the theory.

This procedure does not apply to short-range induction forces which do not follow the macroscopic fluctuation–dissipation theorem; the calculation of their first and second cumulants requires microscopic response functions.⁵⁸ The main consequence is that the induction component does not factorize into temperature and a weakly temperature-dependent energy parameter. The result is a generally non-Arrhenius form of the rate constant⁵¹ in eq 3 in which the variance can be written as

$$C_X(0) \approx 2k_B T \lambda^C + C^{\text{ind}}(0) \quad (16)$$

Since the Coulomb and induction interaction sum up in the energy gap, a cross-term needs to be taken into account, and we have included it in $C^{\text{ind}}(0)$ as follows

$$C^{\text{ind}}(0) = \langle (\delta E^{\text{ind}})^2 \rangle + 2\langle \delta E^C \delta E^{\text{ind}} \rangle \quad (17)$$

Despite these complications which take away the solid foundation behind factoring the variance into the temperature and energy components,^{64,65} we will follow the established tradition and define the solvent reorganization energy as the sum of induction and Coulomb terms (*cf.* to eq 6)

$$\lambda_s = \lambda^{\text{ind}} + \lambda^C \quad (18)$$

where

$$\lambda^{\text{ind}} = C^{\text{ind}}(0)/(2k_B T) \quad (19)$$

The probability of electron transfer can be affected by intramolecular vibrations of the solute.¹¹ These can be added to the formalism outlined here by summing up probabilities of transitions between separate vibronic channels. These transitions are known to significantly affect the transition probability in the inverted region, $\langle \Delta E \rangle < 0$ but can be neglected for transitions in the normal region, $\langle \Delta E \rangle > 0$, considered here. An extension

to the former case is well developed in the literature¹¹ and does not pose fundamental difficulties.

B. Stokes Shift Dynamics. The characteristic time scales of nuclear fluctuations affecting charge transfer can be extracted from the time correlation function in eq 2, or from its normalized value known as the Stokes shift correlation function

$$S(t) = C_X(t)/C_X(0) \quad (20)$$

As mentioned above, the typical shape of $S(t)$ in complex condensed media includes a fast Gaussian component and a multiexponential (or stretched-exponential) tail. A two-exponential tail is used to fit our simulation results with $C_X(t)$ in the form

$$C_X(t) = C^{\text{ind}}(t) + C^C(t) \quad (21)$$

where

$$C^C(t) = 2k_B T [\lambda_G^C e^{-(t/\tau_G)^2} + \lambda_1^C e^{-t/\tau_1} + \lambda_2^C e^{-t/\tau_2}] \quad (22)$$

Here, τ_G is the relaxation time of the Gaussian decay and τ_1 and τ_2 are two exponential relaxation times. In addition, λ_G^C and λ_i^C are the corresponding reorganization energy components such that $\lambda^C = \lambda_G^C + \lambda_1^C + \lambda_2^C$.

C. Nonergodic Activation Kinetics. The arguments presented in section II.A are based on equilibrium statistical mechanics representing the components of the activation barrier as equilibrium (free) energies. This formulation in fact assumes a certain separation of time scales; that is, the time of the reaction $\tau_{\text{ET}} = k_{\text{ET}}^{-1}$ must be much longer than all relaxation times (τ_G , τ_i , etc.) of the nuclear modes coupled to the transferred electron. This assumption certainly breaks down for our problem combining the extremely short time of natural primary charge separation (ca. 3 ps) with the disperse relaxation spectrum of the protein/water solvent.^{13,30,66,67} What we face here is the obvious case of ergodicity breaking⁶⁸ of the nuclear fluctuations involved in the reaction activation, which raises the question of how to approach the calculation of the reaction rates.

The Stokes shift correlation function provides a consistent approach to formulate the kinetics of nonergodic electron transfer. We first note that the equilibrium linear response function, introduced in section II.A in the direct space domain, can be extended to the time domain to cover the time correlation functions of the energy-gap fluctuations. The equilibrium ensemble average producing the solvent response component of the average energy gap (*cf.* to eq 9) can then be given as a frequency integral of the Fourier transform $\chi(\omega)$

$$\Delta E_r^C = -2 \int_0^\infty d\omega \mathbf{E}_{01} * \chi(\omega) * \Delta \mathbf{E} \quad (23)$$

This representation offers a systematic approach to calculating the nonergodic solvent response. The integral in eq 23 is over all possible frequencies of nuclear motions, implying that all of them contribute to the average. In fact, the time scale of the reaction τ_{ET} limits the frequency spectrum only by those frequencies that are higher than the rate of the reaction k_{ET} . The nonergodic energy gap thus becomes

$$\Delta E_r^C(k_{\text{ET}}) = -2 \int_{k_{\text{ET}}}^\infty d\omega \mathbf{E}_{01} * \chi(\omega) * \Delta \mathbf{E}_0 \quad (24)$$

Along the same lines, the nonergodic reorganization energy can be defined by using the same stepwise frequency filter:

$$\lambda^C(k_{\text{ET}}) = \int_{k_{\text{ET}}}^\infty d\omega \Delta \mathbf{E}_0 * \chi(\omega) * \Delta \mathbf{E}_0 \quad (25)$$

An alternative representation is through the Fourier transform of the Stokes shift correlation function

$$C_X^C(\omega) = \int_{-\infty}^{\infty} e^{i\omega t} C_X^C(t) dt / (2\pi) \quad (26)$$

as follows⁶⁹

$$\lambda^C(k_{\text{ET}}) = \beta \int_{k_{\text{ET}}}^{\infty} C_X^C(\omega) d\omega \quad (27)$$

where $\beta = 1/(k_B T)$. Equations 24–27 suggest that $\lambda^C(k_{\text{ET}})$ can be obtained from the Stokes shift correlation function calculated from MD trajectories while a formal theory is required for $\chi(\omega)$ to determine $\Delta E_r^C(k_{\text{ET}})$.

The notion that the parameters entering the activation barrier become functions of the electron-transfer rate creates the necessity to consider the calculation of the rate constant as a self-consistent problem given as the solution of the following equation:

$$k_{\text{ET}} = \omega_e(k_{\text{ET}}) \exp[-\langle \Delta E(k_{\text{ET}}) \rangle^2 / 2C_X(0, k_{\text{ET}})] \quad (28)$$

Here, the rate-dependent energy gap can be rewritten on the basis of eq 24 as

$$\langle \Delta E(k_{\text{ET}}) \rangle = \Delta E^{\text{gas}} + \Delta E^{\text{ind}} + \Delta E_{\text{inh}}^C + f_{\text{ne}}^C(k_{\text{ET}}) \Delta E_r^C \quad (29)$$

where, based on our simulations discussed below, we assume that the induction component of the shift does not involve slow relaxation and only Coulomb solvation gets cut off by breaking ergodicity. Accordingly, the Gaussian width in eq 28 takes the form

$$C_X(0, k_{\text{ET}}) = C^{\text{ind}}(0) + 2k_B T \lambda^C(k_{\text{ET}}) \quad (30)$$

where

$$\lambda^C(k_{\text{ET}}) = f_{\text{ne}}^{\lambda}(k_{\text{ET}}) \lambda^C \quad (31)$$

In eqs 29 and 31, we have introduced the parameters of nonergodicity of nuclear fluctuations contributing to the vertical energy gap, f_{ne}^C , and to the reorganization energy, f_{ne}^{λ} . The parameter f_{ne}^{λ} can be readily calculated from eqs 21, 22, and 27:

$$f_{\text{ne}}^{\lambda} = \lambda_G^C / \lambda^C + (2/\pi) \sum_{i=1,2} (\lambda_i^C / \lambda^C) \cot^{-1}(k_{\text{ET}} \tau_i) \quad (32)$$

The procedure outlined above can be used to construct the free-energy surfaces of electron transfer. The widely accepted definition of the free-energy surfaces for electron transfer follows the general procedure of defining the Landau functional⁶⁴ in which the hypersurface $X = \Delta E$ generates the incomplete partition function

$$e^{-\beta G(X)} \propto \int \delta(\Delta E - X) e^{-\beta H} d\Gamma \quad (33)$$

In this expression, ΔE depends on all nuclear modes Q_n , $n = 1, \dots, M$, in the system. In addition, H is the system Hamiltonian in the initial state of the electron-transfer system and $d\Gamma$ is the element of phase space.

In applications to processes happening on short time scales, one needs to generalize eq 33 to exclude a subset of frequencies not contributing to the process, thus producing a restricted trace:⁶⁸

$$e^{-\beta G(k_{\text{ET}}, X)} \propto \int \delta(\Delta E - X) e^{-\beta H} \prod_{n, \omega < k_{\text{ET}}} \delta[Q_n(\omega)] d\Gamma \quad (34)$$

In this equation, the product of delta functions eliminates the low-frequency modes from the partition function.

D. Polarizability of the Special Pair. There is a significant body of experimental^{70–73} and computational^{135,74–78} evidence

of a strong mixing of covalent, $(P_L - P_M)^*$, and charge-transfer, $(P_M^+ - P_L^-)^*$, states within the photoexcited special pair, where P_M and P_L are the M and L subunits of the special pair (Figures 2 and 3). Although the average amount of charge transfer between two subunits is small,⁷⁵ about 0.1 of the electronic charge in the gas phase and 0.2 in the reaction center, the fluctuations of the electrostatic potential of the protein/water solvent create significant fluctuations of the extent of charge transfer. Correspondingly, the fluctuating population of the charge-transfer state $(P_M^+ - P_L^-)^*$ creates fluctuating charges $\Delta z_j = n_{\text{CT}} \Delta Z_j$ at the atomic sites of the special pair (j runs over the atoms of P). In this representation, ΔZ_j are the difference of atomic charges of the special pair between the ionized excited state $(P_M^+ - P_L^-)^*$ and the covalent state $(P_L - P_M)^*$, and n_{CT} is the population of the charge-transfer state.

Physically, this redistribution of charge in response to an external electrostatic field implies that the special pair is polarizable with the instantaneous induced dipole moment equal to $\mathbf{p}_{\text{CT}} = n_{\text{CT}} \Delta \boldsymbol{\mu}_{\text{CT}}$. Here, $\Delta \boldsymbol{\mu}_{\text{CT}}$ is the dipole moment between the ionized and neutral states of the special pair. The importance of the induced dipole moment for electron transfer is that the instantaneous electron-transfer dipole becomes modified from the dipole $\boldsymbol{\mu}_{\text{ET}}$ created by the set of permanent charges Δq_k (k runs over all atoms of the cofactors involved in electron transfer) to a new fluctuating dipole moment $\boldsymbol{\mu}_{\text{ET}} + \mathbf{p}_{\text{CT}}$. Since the solvent reorganization energy is proportional to the average squared dipole moment

$$\lambda^C \propto \langle (\boldsymbol{\mu}_{\text{ET}} + \mathbf{p}_{\text{CT}})^2 \rangle \quad (35)$$

the appearance of the induced dipole can potentially modify the energetics of electron transfer.^{39–41}

In order to model the effect of polarizability of the special pair on the statistics of the donor–acceptor energy gap, we have adopted the following simulation algorithm. The charges z_j of the special pair are recalculated at each fifth MD step according to the equation

$$z_j = z_j^P + n_{\text{CT}} \Delta Z_j \quad (36)$$

where z_j^P are the charges of two decoupled bacteriochlorophylls obtained from our DFT calculations (Appendix B and Supporting Information). The extent of charge delocalization n_{CT} is calculated by diagonalizing, at each fifth step of the MD trajectory, the two-state quantum Hamiltonian characterized by the electronic coupling J and the instantaneous energy gap between two states

$$\Delta \epsilon = \Delta \epsilon^{\text{gas}} + \Delta \epsilon^{\text{ind}} + (1/2) \sum_j \Delta Z_j \phi_j \quad (37)$$

Here, $\Delta \epsilon^{\text{gas}}$ is the gas-phase energy separation between the neutral and ionized states of P and ϕ_j is the electrostatic potential of the surrounding protein/water solvent at the position of atomic charge j . $\Delta \epsilon^{\text{ind}}$ in eq 37 is the induction shift of the energy gap, and the parameters $\Delta \epsilon^{\text{gas}}$ and J are tabulated in Appendix B.

E. Polarizable Special Pair and Free-Energy Surfaces of Electron Transfer. The description of Coulomb solvation presented in section II.A changes significantly when the special pair is polarizable.^{39,40} The main modification here is that the atomic charges and hence the electric field of the cofactors become a function of the solvent polarization \mathbf{P} through the extent of charge delocalization n_{CT} . The electric field \mathbf{E}_{01} changes from the value commonly calculated from the vacuum charge distribution to $\mathbf{E}_{01}[\mathbf{P}]$:

TABLE 1: Components of the Average Energy Gap for Primary Charge Separation (All Energies Are in eV)

protocol	<i>T</i> , K	ΔE_w^C	ΔE_{prot}^C	ΔE^C	ΔE_w^{ind}	$\Delta E_{\text{prot}}^{\text{ind}}$	ΔE^{ind}	ΔE_s
S1	77	0.170	−0.500	−0.330	−0.058	−1.234	−1.292	−1.623
	200	0.144	−0.728	−0.584	−0.057	−1.199	−1.256	−1.840
	250	0.382	−0.749	−0.367	−0.054	−1.183	−1.237	−1.604
	300 ^a	0.205	−0.678	−0.473	−0.055	−1.164	−1.219	−1.691
	300 ^b	−0.365	−1.278	−1.643	−0.082	−1.071	−1.153	−2.796
	350	0.440	−0.856	−0.416	−0.050	−1.094	−1.144	−1.559
	400	0.093	−0.330	−0.237	−0.075	−0.853	−0.928	−1.164
S2	250	0.399	−0.502	−0.103	−0.048	−1.042	−1.090	−1.193
	275	0.404	−0.535	−0.131	−0.051	−1.065	−1.116	−1.247
	300 ^c	0.310	−0.632	−0.323	−0.052	−1.076	−1.128	−1.451
	325 ^c	0.310	−0.168	0.141	−0.020	−0.836	−0.857	−0.716
	350 ^c	0.347	−0.594	−0.247	−0.053	−0.987	−1.041	−1.287

^a Obtained from 10 ns long MD trajectories, the unmarked data refer to 5 ns of simulations. ^b Data for the final charge-transfer state $P^+ - B_L^-$, 5 ns trajectory. ^c Obtained from 15 ns long MD trajectories.

$$\mathbf{E}_{01} \rightarrow \mathbf{E}_{01}[\mathbf{P}] \quad (38)$$

A general solution for the free energies of electron transfer in this case has not been found so far, although an analytical theory can be formulated in the case of dipole solvation.⁷⁹ Alternatively, the field $\mathbf{E}_{01}[\mathbf{P}]$ can be linearly expanded in the solvent polarization \mathbf{P} around its equilibrium value

$$\mathbf{E}_{01}[\mathbf{P}] = \mathbf{E}_{01}[\mathbf{P}_{\text{eq}} + \mathbf{P}_{\text{eq}}'] + \mathbf{F} \cdot \delta \mathbf{P} \quad (39)$$

where \mathbf{F} is a 2-rank tensor and $\delta \mathbf{P} = \mathbf{P} - \mathbf{P}_{\text{eq}} - \mathbf{P}_{\text{eq}}'$.

When the form of the field given by eq 39 is substituted into the standard Hamiltonian⁵³ of the solute linearly coupled to the Gaussian field \mathbf{P} , one gets

$$H = -\mathbf{E}_{01}[\mathbf{P}_{\text{eq}} + \mathbf{P}_{\text{eq}}'] \cdot \mathbf{P} + (1/2) \delta \mathbf{P} \cdot \chi_{\text{mod}}^{-1} \cdot \delta \mathbf{P} \quad (40)$$

where $\chi_{\text{mod}}^{-1} = \chi^{-1} - 2\mathbf{F}$ is the new, modified linear response function of the Gaussian polarization field renormalized by the solute polarizability. Since the polarizability tensor \mathbf{F} is generally different in the initial and final electronic states, the donor–acceptor energy gap becomes a bilinear function of the Gaussian field \mathbf{P} in contrast to the linear function used to derive the Marcus parabolas. The main consequence of that change is that the statistics of energy-gap fluctuations become non-Gaussian. The free-energy surface loses its parabolic shape predicted by Marcus theory and can instead be represented by the analytical results of the Q-model.⁸⁰

$$G(X) = \alpha (\sqrt{\langle \Delta E \rangle - \alpha \lambda^C - X} - \sqrt{\alpha \lambda^C})^2 \quad (41)$$

Here, $\alpha > 0$ is the non-parabolicity parameter describing the deviation of the free-energy surface from the parabolic shape. The limit $\alpha \rightarrow \infty$ recovers the Marcus barrier thermodynamics.

III. Results

We believe that this paper reports the most extensive MD simulations on the bacterial reaction center following previous simulation efforts in this field.^{27,48,66,81–84} The overall length of 118 ns of MD trajectories, of which 100 ns were used for the production analysis, required 39.8 CPU years. All simulations were done in parallel using 128 CPUs of ASU’s HPC facility. The analysis of the simulations was performed by a parallel code developed for this project that reads directly binary AMBER files. The analysis was run in parallel on 10 Opteron CPUs and required overall 4.8 years of CPU time.

Two sets of simulations have been done. The first set, which we will label S1, was performed at six different temperatures. It employed the standard protocol of MD force fields with fixed atomic charges. The equilibrium MD trajectories were used to

calculate the statistics of the donor–acceptor energy gap and the Stokes shift correlation functions. In this calculation, in addition to Coulomb interactions, induction solute–solvent interactions were computed. The atomic polarizabilities were taken from a modified Thole parametrization⁸⁵ (see Supporting Information for more detail). The induction potential was not a part of the simulation algorithm, thus assuming that the exploration of the phase space of the nuclear motions can be accomplished with the standard force fields. Since these force fields effectively incorporate polarizability in terms of permanent charges, in order to avoid double counting, the charges of the solvent (protein and water) were multiplied by 0.89 in analyzing the data, following the convention adopted in the literature.⁸⁶

Six trajectories of S1 protocol were produced for the initial state of the reaction complex, $(P - B_L)^*$, at different temperatures. The atomic partial charges calculated by us at the DFT level (Appendix B) were supplemented by the force-field parameters of bacteriochlorophyll developed by Marchi and co-workers.⁸⁷ The atomic charges of the ground-state bacteriochlorophyll were used for the excited state of the special pair assuming that photoexcitation does not greatly alter the charge distribution.⁶⁶ One simulation trajectory at 300 K was produced for the charge-separated state $P^+ - B_L^-$ corresponding to the first hop of the electron in the sequential mechanism. For this simulation, the positive charge of P^+ was distributed among the two cofactors of the special pair as described in Appendix B and the charge distribution of the bacteriochlorophyll anion was calculated at the DFT level (Supporting Information).

The second set of simulations, labeled as S2, required changing the standard MD protocol (see Appendix B). In these simulations, quantum polarizability of the special pair was accounted for by diagonalizing the 2×2 Hamiltonian matrix of the charge-transfer state between the two parts of P at each fifth step of the MD trajectory, a procedure known in the literature as the empirical valence bond approach.^{88,89} The Hamiltonian diagonalization allows one to calculate the extent of charge transfer between two bacteriochlorophylls in P and dynamically adjust charges of the special pair. This simulation protocol thus incorporates an extremely high polarizability of P^* revealed by Stark spectroscopy measurements of Boxer and co-workers.^{38,70}

A. Energetics. Two energy parameters are of main importance within the Gaussian picture of electron-transfer activation (Marcus model). These are the average donor–acceptor energy gap and the energy-gap variance (eq 3). These parameters, obtained from MD simulations at different temperatures, are listed in Tables 1 and 2. The complete set of first cumulants

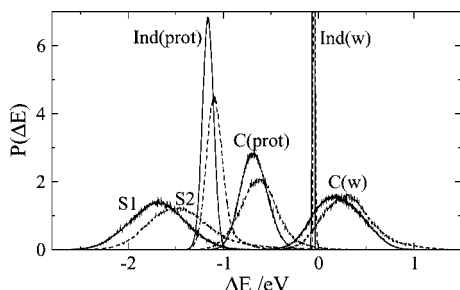


Figure 4. Normalized distributions of components of the donor-acceptor energy gap in nonpolarizable (S1, solid lines) and polarizable (S2, dashed lines) simulation protocols ($T = 300$ K). Marked in the plot are the Coulomb interaction due to the protein ($C(\text{prot})$) and water ($C(w)$) and the induction interaction ($\text{Ind}(\text{prot})$ for the protein and $\text{Ind}(w)$ for water). S1 and S2 mark the distributions of the total energy gap for the nonpolarizable (S1) and polarizable (S2) special pair.

from both S1 and S2 simulations is reported in Table 1. The S2 entry in Table 2 is limited to 300 K, since the second cumulants at other temperatures did not converge on the time scale of the simulation trajectories.

Since we are dealing here with a heterogeneous solvent composed of a protein matrix and aqueous environment, the separation of these two first cumulants of the energy gap into the water and protein contributions provides mechanistic insights into the factors influencing electron-transfer activation. In addition, we split the relevant energies into contributions from nonpolar and Coulomb interactions. Finally, the introduction of polarizability (charge fluctuations) of the special pair shifts relative weights of each component in the activation barrier and, more importantly, results in significant deviations from the Gaussian picture of Marcus parabolas.

Figure 4 reports the distribution of Coulomb and induction components of the energy gap from simulations of both the nonpolarizable and polarizable special pair. The Coulomb interactions have Gaussian statistics where the width is consistent with the reorganization energies listed in Table 2. The average shifts arising from water and the protein have opposite signs. Therefore, the polarization of water by the protein matrix contributes to the destabilizing of the charge-transfer state, as was also observed by Parson et al.⁶⁶ On the contrary, the protein matrix makes the dominant contribution into stabilizing the charge-separated state. The induction shift of the average energy gap, arising primarily from the protein matrix ($\text{Ind}(\text{prot})$ in Figure 4), is about 2 times larger than the Coulomb shift which largely cancels out between its protein and water contributions (Table 1). On the contrary, the width of the distribution of induction energies is small relative to the Coulomb interactions for nonpolarizable (S1) simulations (in accordance with assessment of analytical theories⁵⁸) but grows significantly for the polarizable (S2) simulation protocol (Table 2).

The splitting of the total self-correlation function $C_X(0)$ into the individual protein (subscript “prot”) and water (subscript “w”) components requires an estimate of the cross-correlation term $\lambda_{w,\text{prot}}$ between the water and protein interaction potentials:

$$\lambda_s = \lambda_{\text{prot}} + \lambda_w + \lambda_{\text{prot},w} \quad (42)$$

This latter part turns out to be significantly smaller than the individual protein and water components, as can be inferred from the last three columns in Table 2 by comparing the total solvent reorganization energy λ_s with the sum of the two components, $\lambda_{\text{prot}} + \lambda_w$.

Notwithstanding such little attention paid in the electron-transfer literature to nonpolar interactions, the induction shift is the main part of the solvent effect on the average energy gap of charge separation. Its value can be estimated from some simple arguments. If one assumes that atomic polarizabilities are distributed with a constant density around the donor and acceptor, one arrives at a simple expression⁵⁹

$$\Delta E_{\text{prot}}^{\text{ind}} = -3e^2 \frac{n_{\text{prot}}^2 - 1}{n_{\text{prot}}^2 + 2} \left(\frac{1}{2R_D} + \frac{1}{2R_A} - \frac{1}{R_{DA}} \right) \quad (43)$$

Here, R_D and R_A are the radii of the donor and acceptor and R_{DA} is the distance between them. In addition, n_{prot} is the refractive index of the protein matrix and e is the elementary charge. For the average refractive index of the reaction center⁹⁰ $n_{\text{prot}} = 1.473$ and the radius of the bacteriochlorophyll unit $R_D = R_A = 5.6$ Å obtained from its vdW volume, one gets $\Delta E_{\text{prot}}^{\text{ind}} = -1.09$ eV at the crystallographic distance $R_{DA} = 11.3$ Å. This number compares favorably with the induction shift of $\Delta E_{\text{prot}}^{\text{ind}} = -1.16$ eV from MD simulations at $T = 300$ K (Table 1, S1 protocol).

The positive temperature slope of the induction shift of the average energy gap is caused by the temperature expansion of the protein. On the basis of the data shown in Table 1 for the S1 simulation protocol, the logarithmic derivative of the induction shift with temperature, $d \ln \Delta E_{\text{prot}}^{\text{ind}} / dT$, is within the limits $(4-8) \times 10^{-4} \text{ K}^{-1}$. According to eq 43, this derivative should be equal to thermal expansivity of the protein (Clausius–Mossotti equation). Indeed, the logarithmic slope of the induction shift agrees reasonably well with the reported⁹¹ expansion coefficients of proteins of the order of $8 \times 10^{-4} \text{ K}^{-1}$.

Several of the MD simulation results reported here turned out to be quite surprising. Among the unexpected findings are quite large values of the solvent (protein and water) reorganization energies, contrasting the commonly low values (ca. 0.1–0.2 eV) circulating in the literature.^{10,66,82,84,92} In particular, water is far from being screened by the protein,⁹³ making the main portion of the energy-gap variance in the S1 protocol, and being surpassed by the protein in the S2 protocol. In fact, the values of water reorganization energy found here are more typical of

TABLE 2: Reorganization Energies Calculated from Fluctuations of the Energy Gap (eq 15) (All Energies Are in eV)

protocol	T , K	λ_w^{ind}	$\lambda_{\text{prot}}^{\text{ind}}$	λ^{ind}	λ_w^{C}	$\lambda_{\text{prot}}^{\text{C}}$	λ^{C}	λ_w	λ_{prot}	λ_s^a
S1	77	0.019	0.065	0.070	0.187	0.168	0.351	0.191	0.245	0.421
	200	0.001	0.057	0.062	0.756	0.182	0.845	0.756	0.251	0.903
	250	0.016	0.076	0.081	1.634	0.341	1.938	1.639	0.419	1.955
	300 ^b	0.047	0.112	0.119	1.136	0.375	1.564	1.124	0.466	1.598
	300 ^c	0.047	0.146	0.149	1.393	0.441	1.542	1.379	0.593	1.692
	350	0.110	0.187	0.191	0.948	0.644	1.508	0.944	0.853	1.508
	400	0.139	0.249	0.275	0.767	0.567	1.010	0.866	0.797	1.335
S2	300	0.481	0.682	0.697	1.439	0.735	1.839	1.454	1.385	2.513

^a $\lambda^{\text{ind}} + \lambda^{\text{C}}$ deviates slightly from λ_s because of numerical uncertainties of averaging. ^b Obtained from 10 ns long MD trajectories; the unmarked data refer to 5 ns of simulations. ^c 5 ns data for the final charge-transfer state $\text{P}^+ - \text{B}_L^-$.

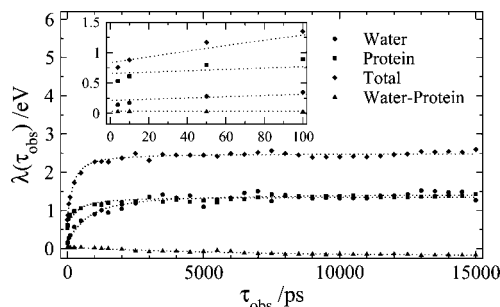


Figure 5. Components of the solvent reorganization energy from water and protein from MD simulations vs the observation time τ_{obs} . The points refer to MD data (S2 protocol, 300 K), and the dotted lines indicate the fits to eq 44. The inset shows the initial portion of the plot; the relaxation times used to fit the MD results to eq 44 are $\tau_R = 218$ ps (total), $\tau_R = 390$ ps (protein), and $\tau_R = 764$ ps (water).

small redox couples in aqueous solution⁹⁴ than of the often anticipated hydrophobic screening by the protein matrix.

What is different in our simulations compared to previously reported simulation data^{66,82,84} is the length of the simulation trajectory which has allowed us to push the numbers for the reorganization energies closer to their thermodynamic limit. Indeed, as is seen in Figure 5, the reorganization energy as a function of the length of the simulation trajectory (observation time τ_{obs}) levels off by the end of the 5–10 ns production run. However, this long-time reorganization energy is not relevant for the short-time charge-separation dynamics, since a significant subset of nuclear modes gets dynamically arrested on the picosecond time scale at which the reorganization energy as a function of τ_{obs} starts to sharply decline (Figure 5). The dependence of the total reorganization energy and its components on the observation window can be fitted to a one-component Debye equation (*cf.* to eq 32)

$$\lambda(\tau_{\text{obs}}) \propto \cot^{-1}(\tau_R/\tau_{\text{obs}}) \quad (44)$$

with the effective relaxation time τ_R . The fits shown by dotted lines in Figure 5 indicate that the system starts to lose ergodicity on the time scale of several hundred picoseconds.

The data in Figure 5 have been generated according to the following procedure. First, a trajectory of individual protein/solvent vertical energies is created from the sum of their respective Coulomb and induction components (Supporting Information). Second, a smaller trajectory window of length τ_{obs} is cut from the full MD trajectory. Third, the energy-gap variance is calculated on this smaller observation window which is then moved along the entire trajectory. Each time the window is shifted, the variance is calculated with the average energy gap set to its average on that particular window. The individual variances are then averaged among the results from each sliding window, and the average reorganization energy is reported as $\lambda(\tau_{\text{obs}})$ in Figure 5.

Reorganization energies calculated from this algorithm are plotted vs temperature in Figure 6. As in Figure 5, shortening the observation window lowers the reorganization energy. On the 4 ps observation window, most of the multiexponential Stokes shift relaxation is dynamically arrested (see below) and only ballistic Gaussian relaxation from the Coulomb interactions and the modulation of induction interactions by density fluctuations contribute to the reorganization energy. For this short observation time, the reorganization energy falls in the range of values commonly reported from fitting the experimental reaction rates.^{10,92}

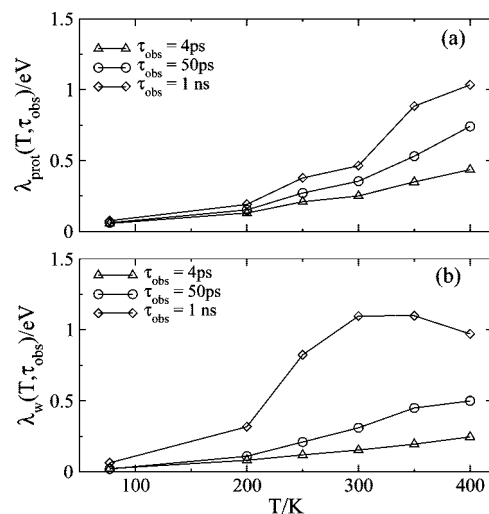


Figure 6. Protein (a) and solvent (b) reorganization energies from MD simulations as functions of the observation time τ_{obs} and temperature.

We need however to note that the reorganization energies observed in these simulations are uniformly higher than those reported in previous simulations of primary charge separation: 0.069 eV by Parson et al.⁶⁶ (40 ps trajectory), 0.2 eV by Treutlein et al.⁸² (20 ps trajectory). These numbers, corresponding to short observation times, are roughly consistent with Figure 6 given that our algorithm of sliding window generally gives higher reorganization energies than a single observation. Our reorganization energies from longer observation windows are however still significantly larger than ca. 0.17 eV reported by Ceccarelli and Marchi⁴⁹ from 3.5 ns (2.4 ns analyzed) trajectories. They observed sudden changes in the energy-gap trajectory, and their reorganization energies were calculated from small portions of the trajectory between the flips. Our trajectories instead feature large-amplitude, smooth oscillations (Supporting Information Figure S1), and the values we report refer to the entire fluctuation breadth accumulated for a given observation window.

The reorganization energy from the protein is an increasing function of temperature for all observation windows (Figure 6a). On the contrary, for water reorganization, the negative temperature slope expected from equilibrium statistical mechanics⁹⁵ is reverted by nonergodicity to a positive one (Figure 6b). This effect is caused by a temperature-dependent unfreezing of the nuclear modes when relaxation becomes faster with increasing temperature. The downward turnover of $\lambda(T)$ for the 1 ns observation window (upper curve in Figure 6b) marks the return of the system to equilibrium statistics with the negative slope of $\lambda(T)$ also seen in our previous simulations of a small solute in SPC/E water.⁹⁶

The opposite temperature dependence of the protein and water reorganization energies at long observation windows points to a distinctly different character of the corresponding nuclear modes. While water molecules alter the donor–acceptor energy gap mostly by librational/rotational motions typical of polar liquids, the protein nuclear modes are predominantly vibrational. The temperature dependence of λ_{prot} seems to correlate well with the temperature dependence of atomic displacements of the protein matrix, as is illustrated in Figure 7 where we show the better converged induction reorganization energy along with the total protein reorganization energy. The temperature change of these reorganization energies is compared with mean-square displacements of hydrogens in bacteriorhodopsin obtained from inelastic neutron scattering.⁹⁷

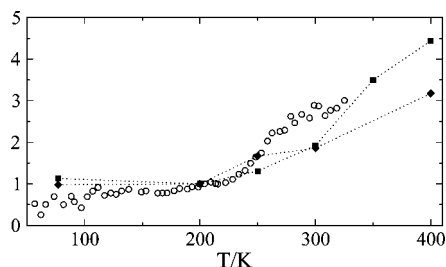


Figure 7. Induction (squares) and total protein (diamonds) reorganization energies from the present MD simulations and experimental mean-square displacements of hydrogens of bacteriorhodopsin scaled with the inverse temperature, $\langle(\delta x)^2\rangle/T$ (circles). The experimental data were obtained by neutron scattering.⁹⁷ All parameters have been normalized to their corresponding values at 200 K.

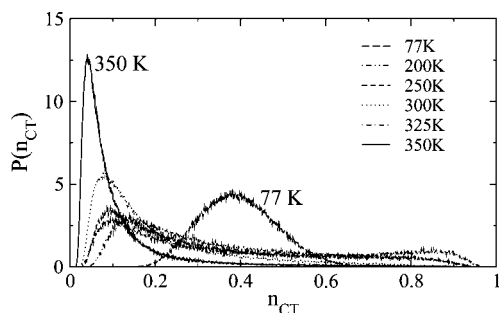


Figure 8. Distribution of the population number of the ionized state of the special pair along the simulation trajectory at different temperatures. The length of the simulation trajectory varies from 5 ns at 77 K to 15 ns at 300, 325, and 350 K.

It is by now well established that protein vibrations start to deviate from the straight line of harmonic motions at the transition temperature of about $T_r \approx 200\text{--}220$ K, marking the rise of anharmonic motions (including side-chain rotations).^{20,97,98} Therefore, the mean-square displacement scaled with inverse temperature, $\langle(\delta x)^2\rangle/T$, is a flat function at low temperatures starting to rise above the transition temperature T_r . The same trend is seen for the total protein reorganization energy and its induction component, which both turn to a sharp increase at about the same temperature. This comparison implies that the relatively large values of protein reorganization energy obtained in our simulations at room temperature can be traced back to highly anharmonic motions of the protein matrix.

B. Polarizable Special Pair. We need to emphasize here that our modeling of the polarizability of the special pair carries qualitative significance only. In addition to the obvious limitations of the two-state model, the modeling of the temperature dependence of the special pair polarizability is not adequate. In our current simulations, the temperature dependence of the average population of the ionized, charge-transfer state of the special pair, $n_{CT}(T)$, originates from the temperature dependence of the diabatic diagonal energy gap (eq 37). This component of the two-state Hamiltonian increases with growing temperature, in general agreement with the idea that a polar environment should become effectively less polar with increasing temperature. Therefore, as is illustrated in Figure 8, the special pair becomes effectively more localized at higher temperatures because the average energy splitting between the two states grows with increasing temperature. The broad distribution of n_{CT} is a signature of the strong vibronic coupling of the charge-transfer state.⁷⁶ What effectively happens due to the strong temperature dependence of the average population is that the polarizability of the special pair is about 400 \AA^3 at $T = 300$ K increasing up to 1800 \AA^3 at 77 K. Given the experimental

temperature variation of the absorption band of the special pair⁹⁹ and the results of Stark spectroscopy at 77 K,³⁸ the former values appear to be more realistic than the latter.

The increase of localization of the special pair in its neutral $(P_M-P_L)^*$ state results in a blue shift of the absorption spectrum in general agreement with experiment.^{99,100} However, the slope of this temperature dependence derived from the data shown in Figure 8 appears to be too large. In vibronic models of the temperature effect on the special pair absorption, this effect is modeled by a temperature-dependent population of vibronic modes coupled to the dimer charge-transfer state.^{78,101} This implies the temperature shift of the diabatic diagonal energy gap. Since this property is determined by the protein/water electrostatic potential in our simulations, a possible way to offset a too strong temperature dependence of absorption frequency is to introduce a temperature-dependent off-diagonal coupling J (Appendix B).⁷⁷ Low-frequency vibrations of the special dimer in the $90\text{--}160 \text{ cm}^{-1}$ region¹⁰² might contribute to that temperature dependence. It seems that the model needs to be modified to reproduce the temperature variation of the absorption spectrum of the special pair. The current simulations in the S2 protocol are therefore not capable of properly addressing the issue of the temperature dependence of the rate. However, we still believe that our results provide valuable insights into how the parameters of the model change once the polarizability is turned on. We therefore report the results of simulations here with the warning that the parameter magnitudes might be modified with the refinement of the model. We will also limit our analysis of the free-energy surfaces of electron transfer to 300 K at which the polarizability seems to be more realistic. What this value at room temperature should be is not entirely clear, since the Stark data were reported at 77 K⁷⁰ (see Appendix B).

C. Free-Energy Surfaces. A general solution for the non-ergodic free-energy surface defined by eq 34 is still missing. The current calculations and analysis of MD data are therefore limited to the phenomenological approach outlined in section II.C where a stepwise frequency filter was introduced into the frequency linear response functions. Computer simulations and comparison to optical experiments in glass-forming liquids support this approach,⁵¹ and one therefore can ask what would be the free-energy surface $G(k_{ET}, X)$ on the time scale of primary charge separation $\tau_{ET} = k_{ET}^{-1}$ compared to the thermodynamic surface $G(X)$.

The thermodynamic free-energy surface is of course not available to us, since sampling is always an issue with simulations. However, leveling off of the reorganization energies on the 10–15 ns trajectory seen in Figure 5 allows us to hope that, except for the slowest modes responsible for the conformational mobility of the protein, the phase space relevant to activating charge separation was adequately sampled. The free-energy surfaces for nonpolarizable (S1) simulations obtained from the 10 ns trajectory for the initial $(P-B_L)^*$ state and from the 5 ns trajectory for the final $(P^+-B_L^-)^*$ state are shown in Figure 9. The results of polarizable (S2) simulations are collected in Figure 10.

Our simulations allow us to sample only the total interaction between the cofactors and the protein/water solvent (eq 6), and therefore, the gas-phase energy gap is missing from the overall energy gap X . This component of the energy gap was obtained from fitting the calculated rate constants at 300 K to the experimental data by Fleming et al.¹ and Wang et al.⁴³ (see below). The gas-phase gap obtained from the fit $\Delta E^{\text{gas}} = 1.86 \text{ eV}$ was used to horizontally shift $G(X)$ obtained from simula-

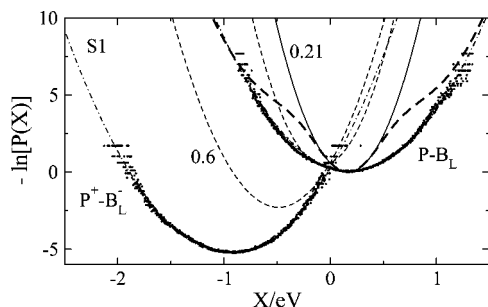


Figure 9. Free-energy surfaces of primary charge separation obtained from MD simulations of the reaction center with the nonpolarizable (constant charges, S1) special pair. The free-energy surfaces $\beta G(X) = -\ln P(X)$ have been obtained from the normalized distributions of the total energy gap X from MD simulations (points) in the initial charge-transfer state, $P-B_L$ (10 ns trajectory), and the final state, $P^+-B_L^-$ (5 ns trajectory). The pair of curves marked with 0.21 are the nonergodic free-energy surfaces calculated by using the $f_{ne}^{\lambda} = 0.21$ value of the nonergodicity parameter following from the fit of the theoretical rate to experiment ($T = 300$ K). The vertical separation of the initial and final free-energy curves is $+97$ cm^{-1} . The vertical separation of -450 cm^{-1} reported by Zinth and co-workers²⁸ is obtained when $f_{ne}^{\lambda} = 0.6$ (marked in the plot) is used in the calculation of the final free-energy curve. The vertical separation between “equilibrium” curves is -1100 cm^{-1} . The dash-dotted lines in the plot are fits to Marcus parabolas yielding equal reorganization energies $\lambda_s \approx 1.6$ eV consistent with direct calculations of second energy-gap cumulants in Table 2. The bold dashed line indicates the free energy obtained by solving the self-consistent nonergodic equation for the rate (eq 28) by varying the average energy gap (see the text). The parameters are those used to calculate the charge-separation rate in Figure 14.

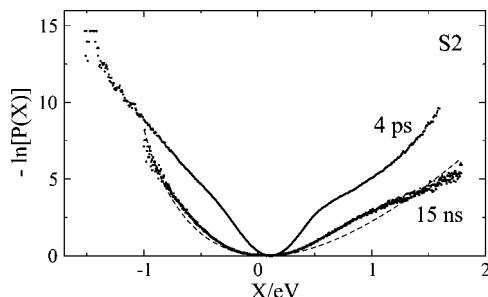


Figure 10. Free-energy surfaces of primary charge separation obtained from MD simulations of the reaction center with the polarizable (fluctuating charges, S2) special pair. The upper curve is obtained from the simulation analysis with a 4 ps observation window, while the lower curve refers to the observation window of 15 ns. The dashed line is the fit of the 15 ns simulation data to the analytical Q-model with the fitting parameters: $\langle \Delta E \rangle = 0.07$ eV, $\lambda_s = 2.81$ eV, and $\alpha = 0.45$.

tions resulting in the average energy gap of $\langle \Delta E \rangle = 0.169$ eV. This number, which is equal to the energetic separation of the free-energy minimum from the point of activationless electron transfer, is consistent with the experimental value of 0.127–0.147 eV (from mutagenesis data) which separates the wild-type reaction center from the top of the Marcus inverted parabola.⁹² Our result is also close to $\langle \Delta E \rangle = 0.150$ eV reported by Wang et al.⁴³ from fitting experimental data to the diffusion-kinetic model (see below).

Long-trajectory simulations in the S1 protocol produce Marcus parabolas (dashed lines in Figure 9) with the curvatures reproducing reorganization energies listed in Table 2. Figure 9 also shows the nonergodic parabolas. Before explaining the calculation of those, we first need to comment on the experimental preparation of the initial state for charge separation. The initial state for primary charge separation is prepared by photoexcitation of the special pair which prior to that stays in

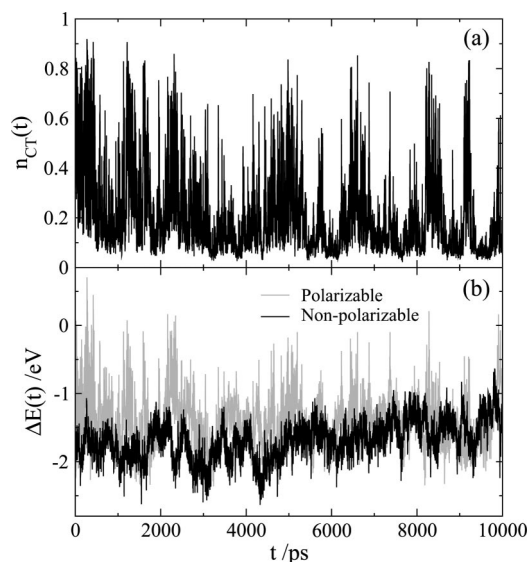


Figure 11. Trajectory of the population of the charge-transfer state of P (a) and the trajectory of energy-gap fluctuations (b) for the nonpolarizable (black line) and polarizable (gray line) special pair.

the ground state for a time long compared to any relaxation time in the system. The ground state is thus characterized by the equilibrium polarization $P'_{eq} + P_{eq}$ of which P'_{eq} is the result of the inhomogeneous protein/water environment and P_{eq} comes from the polarization of the environment by the special pair. When lifted to the excited state by the absorbed photon, the special pair changes its charge distribution and the polarization P_{eq} can dynamically adjust to the new equilibrium polarization P'_{eq} . We will assume that this change, $P'_{eq} - P_{eq}$, is insignificant compared to $P'_{eq} + P_{eq}$ on the reaction time scale. We will therefore neglect the nonergodicity correction in the Coulomb component of the shift assuming $\Delta E^C(k_{ET}) = \Delta E^C$. This approximation results in the following nonergodic free-energy surface

$$G(k_{ET}, X) = \frac{(X - \langle \Delta E \rangle)^2}{4\lambda(k_{ET})} \quad (45)$$

In this equation,

$$\lambda(k_{ET}) = \lambda^{ind} + f_{ne}^{\lambda}(k_{ET})\lambda^C \quad (46)$$

is the nonergodic reorganization energy affected by the dynamical arrest of the Coulomb component of the solvent reorganization. The fit of the rate constant to experiment (see below) results in $f_{ne}^{\lambda} = 0.21$, and the free-energy surface obtained by using this nonergodicity parameter is shown by the solid line in Figure 9.

There is a significant difference between the way the initial and final states for the first electron hop are created. The final state is characterized by an instantaneously created dipole moment of the charge-separated state, and thus, the corresponding Stokes shift requires nonergodic correction with the following result for the final free-energy surface

$$G'(X) = \frac{(X - \langle \Delta E \rangle + f_{ne}'\Delta X_{st})^2}{4\lambda'} + \Delta G_{ne} \quad (47)$$

In this equation, ΔX_{st} is the total Stokes shift between the minima of two parabolas achieved on long simulation trajectories. The nonergodicity parameter f'_{ne} and the reorganization energy λ' depend on both the lifetime of the charge-separated state and the corresponding Stokes shift dynamics. Finally, the

vertical energetic separation between the parabolas' minima ΔG_{nc} (not the reaction free energy) follows from the condition $G(k_{\text{ET}}, 0) = G'(0)$ once all other parameters are known.

We currently do not have sufficient data to calculate the nonergodic parameters in eq 47 (which require, among other things, the free-energy surface corresponding to the electron located at H_L) and so will limit our arguments to qualitative considerations only. The equilibrium free-energy surfaces obtained from long simulation trajectories are vertically shifted by $\Delta G = -1100 \text{ cm}^{-1}$. This number is consistent with experimental data from recombination rates^{12,13} which have put the lowest limit for ΔG at $\approx -2000 \text{ cm}^{-1}$. This later value might be overestimated, since it was measured on the 100 μs lifetime of the triplet state of the special pair. Delayed fluorescent measurements²⁹ sampling the system on the 20 ns time scale and photovoltage measurements at the 15 ns time scale,¹⁰³ both comparable to the length of simulations, show somewhat smaller gaps, $\Delta G_{\text{nc}} \approx -1370$ and -1180 cm^{-1} , respectively. The latter data refer, however, to the *Rhodospirillum rubrum* reaction center.

We need an assignment of f'_{nc} in eq 47 to produce the nonergodic free-energy surface of the charge-separated state. If we use $f'_{\text{nc}} = f_{\text{nc}}^{\text{L}} = 0.21$ from the analysis of the primary charge-separation rate, we get essentially no vertical shift of the two parabolas, $\Delta G_{\text{nc}} = 97 \text{ cm}^{-1}$. The vertical shift of -450 cm^{-1} reported by Zinth and co-workers²⁸ is obtained when $f'_{\text{nc}} = 0.6$ is used in eq 47. This latter value of the vertical displacement of parabolas minima, measured on the picosecond time scale, compares well with the estimate by Holzwarth and Müller,³⁰ -331 cm^{-1} , also done on the picosecond scale. We will postpone a more detailed analysis of the energetics of subsequent electron hops to a future publication, while the current analysis is aimed to show that overall our results do not contradict the key experimental observations reported in the literature. We only note here in passing that, similar to our previous simulations of hydrated plastocyanin,¹⁰⁴ our present simulations show a clear separation between the Stokes shift ΔX_{st} and twice the solvent reorganization energy, $2\lambda_{\text{s}}$ (also see ref 66). We will address this problem in more detail elsewhere.

We need to caution here against a too literal understanding of the nonergodic free-energy surfaces of electron transfer. Under ergodic conditions, the free-energy surface can be sampled by changing the average energy gap by, for instance, optical spectroscopy. The result can then be directly applied to the Franck–Condon factor of the reaction yielding the reaction energy-gap law. In the case of nonergodic reactions, this direct application of the free-energy surface obtained at a given observation window is prohibited, since the spectrum of fluctuations changes at each rate constant achieved by horizontally sliding the free-energy surface and thus sampling the average gap. In order to illustrate that, we have plotted in Figure 9 the free-energy surface obtained by changing the average energy gap in the self-consistent nonergodic equation for the rate constant (eq 28). The result is a funnel-like surface, which we also previously obtained in a study of ergodicity breaking in liquid crystals.¹⁰⁵ The such obtained curve transforms from the narrow free-energy surface at a high reaction rate to the thermodynamic surface when the barrier for the reaction increases and the rate slows down.

As is clear from the broader distribution of energy gaps for the polarizable special pair (Figure 3) and from Table 2 where specific values of the reorganization energies are listed, the free-energy surfaces $G(X)$ are quite different for a polarizable and nonpolarizable special pair. As a matter of fact, not only

curvatures (reorganization energies) are different in two cases, but also, the shape of the free-energy surface changes from a Marcus parabola in the former case to a significantly asymmetric shape in the latter (Figure 10). This result is consistent with the predictions of the Q-model of electron transfer in polarizable donor–acceptor complexes, and in fact, the simulated curve is well fitted to eq 41 (dashed line in Figure 10). Note that the reorganization energy obtained from the fit is close to the result of direct calculation from the second cumulant (eq 15, Table 2).

The increase in the reorganization energy in the case of polarizable P comes from fluctuations of the amount of charge transfer between the covalent and ionized states of P (Figure 11). It is clearly seen from Figure 11 that energy-gap fluctuations in excess to those existing for nonpolarizable P trace the fluctuations of n_{CT} . Most of the excess reorganization energy comes from the protein. The reorganization energy from water actually gets smaller when polarizability is introduced, but the protein reorganization energy is increased by a factor of 4.

We do not currently have an established theoretical algorithm of how to calculate the nonparabolic free-energy surfaces of electron transfer involving highly polarizable donor–acceptor states when ergodicity is broken. In the absence of a theoretical formalism, we have turned to simulations. Figure 10 shows the free-energy surface produced from simulations by sliding the observation window of the length 4 ps along the trajectory and then averaging all the histograms produced from each window after shifting them to a common probability maximum. The normalized distribution produced in this way is then used to plot the nonergodic free-energy curve shown in Figure 10. In contrast to distributions obtained with the nonpolarizable simulation protocol, the nonergodic surface turns out to be nonparabolic. We do not presently have a good explanation of this observation.

D. Charge-Transfer Rates. The decay of the population $P(t)$ of the photoexcited special pair is known to be nonexponential.^{43,106,107} Recent explanations of this observation^{43,108} have cast the problem in terms of the Fokker–Planck kinetics with a Golden Rule reaction sink, similar to formalisms developed in the past by Agmon and Hopfield¹⁰⁹ and Sumi and Marcus.⁴⁴ This theoretical algorithm offers the following physical picture. At the initial time $t = 0$, a laser flash lifts the equilibrium population $P_{\text{eq}}(X)$ of the ground P to the excited-state P* (dashed line in the left panel in Figure 12). At this moment, the state P* is fully occupied, $P(0) = 1$. The system can decay to the charge-separated state with the frequency ω_{e} (eq 4) at the activated state $X = 0$, thus depleting $P(t)$ and changing $P_{\text{eq}}(X)$ to $P(X, t)$ (dash-dotted line in the left panel in Figure 12). At the initial time, $P(X, t) \approx P_{\text{eq}}(X)$, and the decay is determined by the equilibrium rate k_{ET} given by eq 3. However, as the population of the activated state $X = 0$ depletes from that given by the Boltzmann distribution, the continuation of the reaction requires a diffusional supply of the population to the activated state. The result is a slower population decay and effectively multiexponential kinetics. Given that the activation barrier is small for primary charge separation (Figure 9), the diffusional regime kicks in at the early stage of the reaction, leading to observable deviations from monoexponentiality.

Two complications need to be recognized in applying this type of diffusion-reaction kinetics to the problem of primary charge separation. The first complication, well-recognized in studies of the dynamic solvent effect on electron transfer in small molecules,^{46,110} is related to the fact that the Stokes shift dynamics are nonexponential, in particular in its initial Gaussian stage. The common approach to the problem, going back to

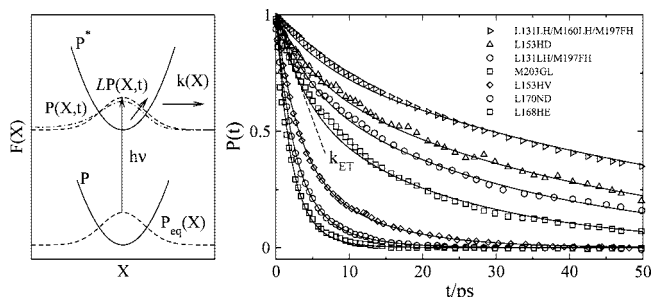


Figure 12. Left panel: Photoexcitation of the special pair lifting the equilibrium distribution (dashed line) from the ground state to the electronically excited state. This excitation starts the decay of the population through the Gaussian sink $k(X)$, along with the one-dimensional diffusion given by the Fokker–Planck operator $LP(x, t)$. The dash-dotted line indicates depletion of the population at the side of the sink, resulting in a slowing down of the population relaxation and in overall nonexponential kinetics. Right panel: Population decays of mutants of the reaction center of *Rhodobacter sphaeroides* taken from ref 43 (points) and fits of $P(t)$ to the diffusion-reaction model (solid lines). The legend in the right panel specifies mutants altering the local electrostatic potential at the special pair.⁹² The dashed line marked k_{ET} shows the initial population decay with the electron-transfer rate constant according to eq 52.

the Sumi–Marcus formalism,⁴⁴ is to split the overall energy gap X into fast, x_f , and slow, x , components, $X = x_f + x$. The evolution operator along the reaction coordinate X is then averaged over the equilibrium distribution of the fast component, resulting in a diffusion-reaction equation for the population along the slow reaction coordinate x only:

$$\partial P(x, t)/\partial t = [L(k_{ET}, x) - k(x)]P(x, t) \quad (48)$$

In this equation, $L(k_{ET}, x)$ is a diffusional operator

$$L(k_{ET}, x) = D(k_{ET}) \frac{\partial}{\partial x} \left[\frac{\partial}{\partial x} + \beta \frac{\partial G(k_{ET}, x)}{\partial x} \right] \quad (49)$$

describing the Fokker–Planck dynamics in the potential given by the electron-transfer free-energy surface. For multiexponential decay, a time-dependent diffusion constant can be used for the harmonic potential $G(k_{ET}, x)$,¹¹¹ while an effective relaxation time τ_{eff} needs to be defined for a general potential. Following Hynes,¹¹² this relaxation time is defined here in terms of a weighted sum of the corresponding rates of exponential relaxation. For a biexponential long-time tail in eq 21, one gets

$$\tau_{eff}^{-1} = (\lambda_1^C \tau_1^{-1} + \lambda_2^C \tau_2^{-1}) / (\lambda_1^C + \lambda_2^C) \quad (50)$$

The diffusion constant in eq 49 then becomes $D(k_{ET}) = 2k_B T \lambda^C(k_{ET}) / \tau_{eff}$. Finally the rate constant $k(x)$ in eq 48 is the Golden Rule rate averaged over the equilibrium distribution of the fast relaxation component

$$k(x) = \omega_e \sqrt{\lambda_s / (\lambda_G^C + \lambda^{ind})} \exp \left[-\beta \frac{(\langle \Delta E \rangle - x)^2}{4(\lambda_G^C + \lambda^{ind})} \right] \quad (51)$$

where λ_G^C is the fast Gaussian component of decay in eq 21, λ^{ind} is the induction reorganization energy, and $\langle \Delta E \rangle$ is given by eq 5.

Most studies applying this formalism in the past have assumed that the overall rate of diffusional reaction, i.e., the rate of arriving at the transition state $X = 0$ from the bottom of the potential well, is much smaller than the relaxation rate of any nuclear mode coupled to electron transfer. This is obviously not true in our case, and nonergodicity corrections, already introduced into eqs 48–51, are required. These corrections

come in the form of the free-energy surface $G(k_{ET}, x)$ depending on the rate k_{ET} (eq 34), as well as the diffusion coefficient $D(k_{ET})$ depending on the nonergodic reorganization energy $\lambda^C(k_{ET})$. Therefore, any solution of the dynamic diffusion-reaction equation should produce a closure for k_{ET} and then solved by repeated iterations.¹⁰⁵ Equation 48 was solved employing the generalized moment expansion of Nadler and Marcus⁴⁵ to produce k_{ET} as the initial population decay (right panel in Figure 9)

$$k_{ET} = - \left. \frac{d \ln P(t)}{dt} \right|_{t=0} \quad (52)$$

where $P(t) = \int P(x, t) dx$. This condition establishes the closure for the self-consistent calculation of k_{ET} by repeated solutions of eq 48. The free-energy surface is then obtained by a horizontal shift of eq 45, $G(k_{ET}, x) = x^2 / [4\lambda(k_{ET})]$.

The approach outlined here results in a good agreement with experimental population decays for a number of mutants reported by Wang et al.⁴³ (Figure 12) with the input parameters produced by the S1 simulation protocol. Also notice that the rate constant in the sink term in eqs 48 and 51 is purely classical and does not incorporate quantum vibrations. For reactions in the inverted region, quantum Franck–Condon vibrational overlaps provide additional vibronic channels for electronic transitions.¹¹³ Primary charge separation appears to operate in the normal region⁹² (Figure 8) and quantum vibrations can be omitted. Notice, however, that classical phonon modes have been included into the fast Gaussian and induction components of the reorganization energy.

The Stokes shift correlation function necessary to calculate the nonergodic reorganization energy from eq 27 at each iteration step in eq 48 was taken from MD simulations of the reaction complex (Figure 13). Several important observations follow from examining Figure 13. The ballistic component of the decay, arising from ballistic motions of water and quasi-lattice vibrations of the protein matrix, is significantly diminished¹¹⁴ compared to the Stokes shift dynamics of small chromophores in water.¹⁶ Indeed, the sum of the Gaussian component of the Coulomb reorganization energy and the induction reorganization energy, both responsible for the fast decay, is below 20% of the overall solvent reorganization energy λ_s . This fact is critical for the analysis of nonergodic free-energy surfaces of electron transfer, as the fast relaxation component is essentially the only part of nuclear reorganization which is not dynamically arrested on the short time scale of charge separation (see below).

The exponential tail of the Stokes shift decay becomes slower with cooling, as expected. The effective relaxation time $\tau_{eff}(T)$ can be calculated from the fitted exponential relaxation times according to eqs 22 and 50 and fits well by an Arrhenius function ($200 \text{ K} \leq T \leq 400 \text{ K}$) with the activation energy of $E_\tau = 1212 \text{ K}$. This activation barrier is close to the value $\approx 1060 \text{ K}$ reported for the long-time tail of the fluorescence decay of an optical probe bound to a protein.¹¹⁵ This activation barrier was assigned to local segmental motions of the protein coupled to the hydration layer. The long tail in the Stokes shift correlation function observed here is, however, shorter than that reported in ref 115 and is in fact close to the slow protein–water dynamics with the characteristic time of $\approx 90 \text{ ps}$ recently reported from Stokes shift data in ref 116.

The combination of the Arrhenius temperature dependence with the low activation energy points to the link between exponential Stokes shift relaxation and β relaxation of the protein/water system. Previous measurements of α relaxation

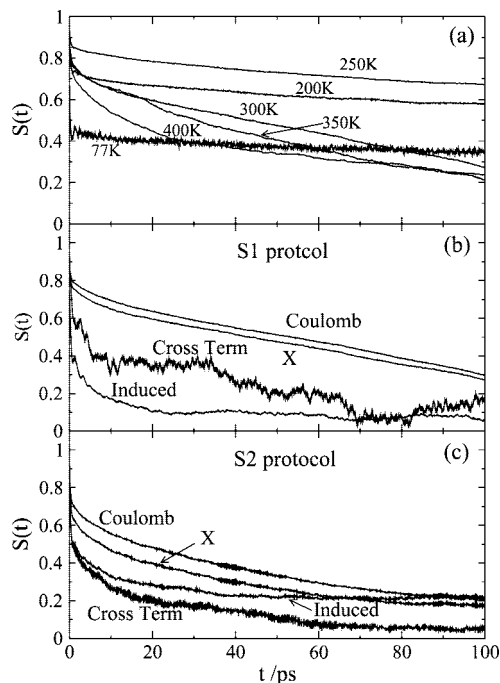


Figure 13. Stokes shift correlation function of primary charge separation obtained from 5–15 ns MD trajectories in S1 and S2 simulation protocols. $S(t)$ at different temperatures with the nonpolarizable special pair are shown in part a. In part b, the overall Stokes shift correlation function at 300 K (marked as X) is compared to its components from Coulomb and induction interactions, along with the Coulomb/induction cross-term (eq 17). In part c, the same separation into components of $S(t)$ is shown for simulations with the polarizable special pair at 300 K.

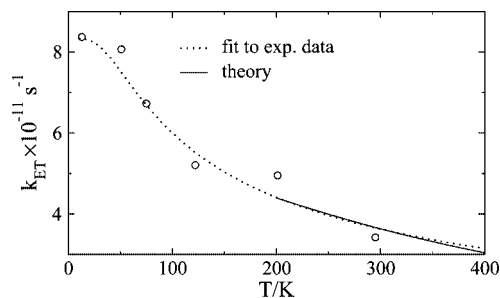


Figure 14. Temperature dependence of the rate of primary charge separation from experiments by Fleming et al.¹ (points) and from calculations of the rate using the gas-phase energy $\Delta E^{\text{gas}} = 1.86$ eV and $V = 41.5$ cm⁻¹ adjusted to reproduce the rate at $T = 300$ K (solid line). The dotted line represents the fit of experimental data to an empirical equation suggested in ref 1.

in hydrated proteins have consistently shown much larger effective activation barriers of the order 6000–9000 K,^{20,117} in addition to the breaking of the Arrhenius law in a broad temperature range. We therefore conclude that primary charge separation is coupled to two nuclear modes: Gaussian ballistic/phonon motions and exponential β relaxation. The relaxation time of the former turns out to be close to 0.1 ps⁸² and is essentially independent of temperature. We note in this regard that anharmonic protein displacements shown in Figure 7 are also linked to β relaxation.²⁰ The decoupling of the Stokes shift dynamics of the primary charge separation from α relaxation is distinct from the situation commonly seen for solvation dynamics of small solutes¹⁷ and, among other things, implies that dielectric α -relaxation data, routinely used to calculate solvation dynamics of small chromophores,²² have little to do with the dynamics of primary charge separation.

TABLE 3: Solvent Reorganization Energies (eV) and Their Water and Protein Components from MD Simulations (The Reorganization Energies Depending on the Reaction Rate Were Obtained from Stokes Shift Dynamics According to eq 27; k_{ET} Refers to the Charge-Separation Rate at the Corresponding Temperature)

protocol	T , K	λ_s	$\lambda_s(k_{\text{ET}})$	λ_w	$\lambda_w(k_{\text{ET}})$	λ_{prot}	$\lambda_{\text{prot}}(k_{\text{ET}})$
S1	77	0.421	0.266	0.191	0.072	0.245	0.210
	200	0.903	0.257	0.756	0.106	0.251	0.201
	250	1.955	0.261	1.639	0.126	0.419	0.235
	300	1.598	0.454 ^a	1.124	0.124	0.466	0.260
	350	2.239	0.657	1.246	0.202	1.407	0.611
	400	1.335	0.639	0.866	0.259	0.797	0.451
S2	300	2.513	1.276	1.454	0.188	1.385	0.970

^a Direct fits of the experimental population decays to the Sumi–Marcus model considering the average energy gap and the reorganization energy as fitting parameters gave $\lambda_s = 0.350$ eV and $\langle \Delta E \rangle = 0.150$ eV.⁴³

Stokes shift dynamics allow us to calculate the nonergodic reorganization energies entering the reaction rates and population decays. Table 3 reveals yet another important mechanistic aspect. It shows that the reorganization energy of water is significantly cut off by the dynamical arrest. Reorganization of fast, anharmonic quasi-lattice vibrations of the protein emerges from the water dominance in the thermodynamic limit, acting as the leading mode driving electronic transitions on the picosecond scale.

We now turn back to the calculation of the rates of primary charge separation. Two types of laboratory experiments are most relevant to our discussion. The first are the measurements by Fleming and co-workers¹ of charge-separation rates in a broad range of temperatures between helium, 5 K, and room temperature, 300 K. The experimental observation, which has puzzled theorists ever since, is a very gentle decay of the electron-transfer rate over the whole temperature range (open points in Figure 14). This result is apparently inconsistent with any conceivable temperature dependence of equilibrium nuclear solvation energies, even if activationless electronic transition is realized at some intermediate temperature. The second set of experimental results, reported by Allen and Woodbury and co-workers,^{42,92} provides population decays of P^* in a carefully engineered set of mutants altering the electrostatic potential at the location of the special pair. A surprising result of these experiments was the realization that the wild-type reaction center falls off the top of the energy-gap law into the normal region of electron transfer.⁹²

Our current calculations, based on the input from MD simulations and the concept of solvation nonergodicity, are capable of reproducing the experimental decay curves $P(t)$ for the whole set of mutants studied by Allen and Woodbury (Figure 12). In the fit, the electron-transfer matrix element was obtained from the 300 K rate of the wild-type reaction center and the inhomogeneous component of the average energy gap ΔE_{inh}^C was varied among the mutants (electrostatic mutations⁹²). The fitted variation of ΔE_{inh}^C is consistent with changes in the midpoint electrochemical potential upon the mutation (Appendix C). In order to further test the consistency of these results with the experimental database, one needs to prove that the experimental rates at different temperatures¹ can be obtained with the set of parameters used to fit the mutagenesis data. These results are shown in Figure 14 with the details of calculations given in Appendix C.

Proper account of the temperature variation of the parameters entering the activation barrier is important in reproducing the

TABLE 4: Parameters Used to Fit the Charge-Separation Rate at 300 K and to Produce the Temperature Dependence of the Rate^a (All Refer to the Parameters Wild-Type Reaction Center; Temperature Derivatives Taken at 300 K Are in K⁻¹)

ΔE^{gas} , eV	V , cm ⁻¹	$d \ln \Delta E^{\text{C}}/dT$	$d \ln \Delta E^{\text{ind}}/dT$	$d \ln \lambda^{\text{C}}/dT$	$d \ln \lambda^{\text{ind}}/dT$
1.86	41.5	5.2×10^{-4}	4.8×10^{-4}	-1.3×10^{-3}	1.1×10^{-2}

^a Temperature dependence of the Stokes shift correlation function was produced by using the following parameters in eq 22: $A_G = 0.172$, $\tau_G = 0.1$, $A_1 = 0.063$, $\tau_1 = 2.5$ ps, $\tau_2^0 = 2.55$ ps, $E_r = 1212$ K with $\tau_2(T) = \tau_2^0 \exp[E_r/(k_B T)]$.

observed rates. The main factor here is the temperature dependence of the induction shift, which is well converged in our simulations and slopes positively with increasing temperature (Table 1). Unfortunately, the accuracy of the current simulations does not allow us to address the temperature dependence of the Coulomb components of the energy shift and reorganization energy, since their changes in the interval of temperatures studied are within the uncertainties of numerical simulations. Our previous experience with another photosynthetic protein, plastocyanin, suggests that the length of the simulated trajectories needs to be extended up to at least 20 ns for a reliable estimate of the temperature slope,¹¹⁸ which is beyond our current computational capabilities. Therefore, in order to assign realistic slopes to the Coulomb components of the free-energy barrier, we used our previous observation^{63,95} that the results of many calculations and experiments on small solutes in polar solvents give the logarithmic slope of the Coulomb reorganization energy in the range $\Delta \lambda^{\text{C}}/\lambda^{\text{C}} \approx -(2-3) \times 10^{-3} \Delta T$. The Coulomb reorganization energy was then assigned the slope of $\Delta \ln \lambda^{\text{C}}/\Delta T = -1.3 \times 10^{-3} \text{ K}^{-1}$ and, based on its relative magnitude, the Coulomb component of the average energy gap was given the slope of $\Delta(\ln \Delta E^{\text{C}})/\Delta T = 5.2 \times 10^{-4} \text{ K}^{-1}$ (see Table 4). These assignments do not affect our results much, since a close fit can also be obtained by assuming these two parameters are temperature-independent. We finally note that the problem of the temperature dependence of the reaction parameters, in particular the driving force, is not free of controversy. Opposite signs of reaction entropy have been obtained for different charge-transfer reactions^{12,119} in the reaction center, and temperature-independent parameters are routinely used in the analysis.^{120,121}

The nonergodic free-energy surface of electron transfer (narrower surface in Figure 10) obtained from simulations with a polarizable special pair can also be used to fit the experimental reaction rate at 300 K. This fit results in the gas-phase gap of $\Delta E^{\text{gas}} = 1.57$ eV used in Figure 10 to plot the free-energy surfaces. This value of the gas-phase gap yields the average energy gap of $\langle \Delta E \rangle = 0.150$ eV, consistent with the experimental evidence⁹² and previous fits of the rates by Wang et al.⁴³ The nonergodic reorganization energy obtained from fitting the curvature at the minimum of the $G(k_{\text{ET}}, X)$ curve turns out to be 0.39 eV, close to the value of 0.46 eV reported for S1 simulations in Table 3 and the value of 0.35 eV reported by Wang et al.⁴³ The nonergodic free-energy curves from Figures 9 and 10 are used to construct the energy-gap law of electron transfer plotted against the variation of the inhomogeneous electrostatic potential of the protein, as was done in mutagenesis experiments.⁹² We find that polarizable and nonpolarizable simulations result in close shapes of the energy-gap law.

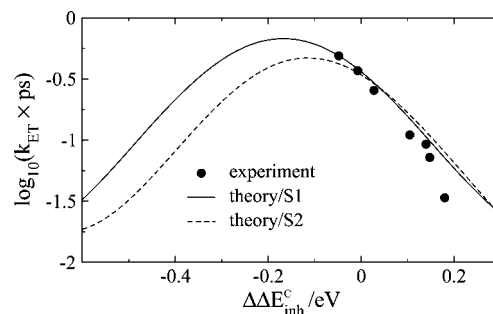


Figure 15. Charge-separation rate vs the variation of the average donor-acceptor energy gap produced by mutagenetic substitution (points⁴³). The lines are obtained by horizontal shifts of the nonergodic parabolas of the initial charge-separation state obtained in the S1 protocol (solid line, Figure 9) and in the S2 protocol (dashed line, Figure 10). In experiment, mutagenetic substitution varies the inhomogeneous part of the Coulomb component of the average vertical gap, and therefore, that parameter marks the horizontal axis; $\Delta \Delta E_{\text{inh}}^{\text{C}} = 0$ corresponds to the wild-type reaction center.

IV. Discussion

A. Mechanism of Electron-Transfer Activation. The extensive MD simulations of the bacterial reaction center combined with formal modeling have allowed us to look closely at the nuclear modes driving electronic transitions and their energetic balance in the reaction activation barrier. Several qualitative results have emerged from our analysis. From the viewpoint of the relative participation of different types of interaction potentials, we have shown that induction and Coulomb forces give comparable contributions to the average energy gap, while Coulomb interactions tend to dominate the reorganization energy of electron transfer. A significant finding of this study is the realization that, on the nanosecond time scale achievable by numerical simulations, the reorganization energies and shifts are quite significant, much larger than had been anticipated so far. The understanding that most of this nuclear solvation is dynamically frozen on the time scale of the reaction then became critical for the quantitative description of the observable rates. While water dominates the reorganization energy on the nanosecond time scale, most of this solvation freezes on the picosecond reaction time scale, and protein vibrations emerge as the main nuclear mode driving electronic transition. Still, there is a noticeable component of water reorganization, originating from the ballistic Gaussian decay of the Stokes shift correlation function, left even on the picosecond time scale (Table 3).

Once the protein is identified as the major heat reservoir operating on the picosecond time scale of the reaction, one can try to identify a particular mode most strongly coupled to the transferred electron and driving the electronic transition. Several answers to this question have been proposed in the past. Wang et al.⁴³ suggested to use transient changes in tryptophan absorbance at 280 nm to monitor the electron-transfer kinetics. In this approach, photoexcited tryptophan serves as a time-resolved probe of the ultrafast nuclear rearrangement of the protein matrix with the hope that the dynamics recorded by spectroscopy will match the Stokes shift dynamics unreachable by spectroscopic techniques. Since both types of information are available from our simulations, we have tested this hypothesis here.

Figure 16 compares the Stokes shift dynamics of primary charge separation with the Stokes shift dynamics of tryptophan averaged over all tryptophans in the reaction center protein. Although these two match each other reasonably well, the

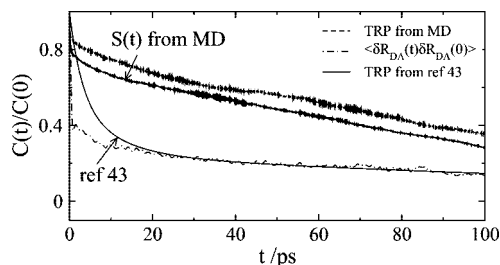


Figure 16. Total Stokes shift correlation function of primary charge separation compared to the Stokes shift correlation of reaction center tryptophans (dashed line) and to the normalized self-correlation function of the fluctuations in the donor-acceptor distance $R_{DA}(t)$ between the special pair and bacteriochlorophyll (dash-dotted line). The lower solid line shows the correlation function of the tryptophan absorbance band taken from ref 43.

experimental trace⁴³ shown in the same plot is quite different, having, in particular, a much faster initial decay.¹²² It turns out that this experimental trace matches quite well the autocorrelation function of the donor-acceptor distance between the special pair and the accessory bacteriochlorophyll cofactor B_L (Figure 2; see also Supporting Information Figures S2 and S3). The decay of this function is also caused by protein vibrations, suggesting that the experimental observation traces one of the long-wavelength vibrational modes responsible for large-scale protein motions but not necessarily the modes contributing primarily to the Stokes shift dynamics of primary charge separation.

In fact, following an early proposal by Gehlen et al.,⁸³ Chaudhury et al.¹⁰⁸ recently suggested that donor-acceptor vibrations represent the mode activating electronic transitions. Our current results do not support this hypothesis. The dynamics of the donor-acceptor vibrations are different from the Stokes shift dynamics. In addition, both the self-correlation function of donor-acceptor distances and the experimental trace of Wang et al.⁴³ produce too large an amplitude of the initial decay which would make a larger portion of nuclear solvation unfrozen on the time scale of the reaction, thus invalidating the analysis of the reaction rates (see below). On the experimental side, related evidence shows the low sensitivity of charge-recombination rates to high pressure (up to 345 MPa) which caused about 16% of volume change of the sample.¹²³

What has not been considered so far in the long history of modeling primary charge separation is the possibility that a high polarizability of the photoexcited special pair can significantly modify the energetics of the reaction. Our simulations here are the first attempt to understand the possible consequences of the gigantic polarizability of the special pair for the charge-transfer energetics and kinetics. The polarizability of the special pair was modeled here by the two-state model^{35,124} with the dynamic adjustment of the population between charge-transfer and neutral states of the special pair along the simulation trajectory. The two-state model has its obvious limitations, and a possibility of a broader spectrum of electronic states^{77,125} can be considered in the future, along with improved modeling of the temperature variation of the absorption spectrum of the special pair. Nevertheless, the present simulations give the first insights into what sort of changes to the energetics should be anticipated when the polarizability has been taken into account.

What we have found here is consistent with previous studies of the role of polarizability in the energetics of electron transfer.^{39,40} The free-energy surface of the initial electron-transfer state involving a polarizable special pair is significantly distorted compared to Marcus parabolas which we obtained in

the simulation protocol with the nonpolarizable primary pair (cf. Figures 9 and 10). The reorganization energy, obtained as the variance of the energy-gap fluctuations, is significantly enhanced compared to the case of nonpolarizable simulations, also in agreement with the previous studies.^{40,126} The free-energy curve could be fitted with the analytical equations of the Q-model, which introduces a nonparabolicity parameter in addition to the two-parameter description of the Marcus model.

Although the free-energy curve from the 15 ns trajectory shown in Figure 10 is perhaps the most asymmetric electron-transfer free-energy surface ever reported from numerical simulations,⁴⁰ most of this asymmetry is washed out by the dynamical arrest of nuclear solvation on the reaction time scale. The free-energy surface narrows down and approaches the Marcus parabola on the 4 ps observation window (Figure 10). In fact, the rate of charge separation can be equally well described by either polarizable or nonpolarizable simulation data with a close range of parameters and a close match between the resulting energy-gap laws (Figure 15). It appears that what charge separation probes on the picosecond observation window is a stripped surrogate of the rich dynamics and thermodynamics of the protein/water electrostatics on the time scale of thermodynamic observables. Nature has therefore played with dynamical time scales to reduce these complexities to a near-resonance electron transfer driven by ballistic phonon motions.

B. Rates of Primary Charge Separation. The ideas of nonergodic nuclear solvation advocated here were tested for consistency with experimental observations by calculating the rates of charge separation as a function of temperature,¹ and the kinetics of the population decay depending on mutagenetic substitution.⁴³ Since the simulation protocol involving the nonpolarizable special pair had produced Marcus parabolas for the free-energy surfaces, we were able to use the diffusion-kinetic model advanced by Sumi and Marcus⁴⁴ in order to calculate the population decay. The main question we were asking here is whether the use of the same set of fitting parameters (electron-transfer matrix element V and the gas-phase energy gap ΔE^{gas}) would provide us with a consistent description of both sets of experiments. We obtained a positive result here (Figures 12 and 14).

A fit of the population decay to the Sumi-Marcus diffusion-kinetic model was also presented by Wang et al.⁴³ In their analysis, the diffusion coefficient was taken to be time-dependent in order to reflect the non-Markovian character of the relaxation.¹¹¹ Both the average energy gap and the reorganization energy were considered as fitting parameters. We found that the use of the time-dependent diffusion coefficient is not a necessity, since the same data can be reproduced with an effective diffusion coefficient extracted from Stokes shift correlation functions. What distinguishes our analysis from theirs is that the solvent-induced shift of the average energy gap and the reorganization energy are fixed by MD simulations, instead of used as fitting parameters. The gas-phase gap and the electron-transfer matrix element were fitted to the rate at 300 K, but then, these parameters allowed us to reproduce Fleming's data. With these restraints on the parameters' magnitudes, there is very little room for adjusting the two parameters. We also note that the results of the calculations, and of our simulations of the charge-separated state $P^+-B_L^-$, are consistent with the current state of experimental evidence regarding the energetics of primary charge separation, as we have discussed in section III.C.

The negative slope of the charge-separation rate with increasing temperature has puzzled theorists for two decades, and has

mostly been approached by considering a temperature-dependent population of phonon modes coupled to electron transfer.¹¹ Although our simulations and conclusions are for the most part limited to high temperatures greater than 200 K, explaining the negative temperature slope of the rate in this region does not require vibronic coupling models. We found the reaction rate to follow the temperature variation of the induction component of the average energy gap which itself becomes less negative with increasing temperature because of the protein expansion.

We have confirmed the observation made by Haffa et al.⁹² that primary charge separation falls into the normal region of electron transfer (Figures 9 and 15). This result was considered incompatible with the weak temperature dependence of the rate, and a vibrational heating mechanism^{92,127,128} was suggested in order to explain the positive $\langle\Delta E\rangle$. Our current calculations suggest that Fleming's data can be reconciled with $\langle\Delta E\rangle \approx 0.15$ eV for the wild-type reaction center without assuming vibrational heating once the temperature dependence of $\langle\Delta E\rangle$ is taken into account. The main component of $\langle\Delta E\rangle$ responsible for its temperature dependence is the shift by electronically instantaneous induction forces which do not get dynamically frozen, but rather changes due to a temperature-affected alteration of the protein's refractive index (eq 43). Our simulations also suggest that the wild-type reaction center is driven even further from the optimum activationless energetics when the temperature increases above the room temperature and that the optimum activationless configuration is reached at around 200 K (Supporting Information Figure S4). We refrain from speculations on evolutionary implementations of this result.

C. Broader Insights. Electron transfer connects cofactors in energetic redox chains in biology. Three parameters are generally believed to have the main impact on the kinetics of electron hops: the redox potential, the probability of tunneling, and the reorganization energy. The first one is relatively well understood, and, in many cases, accessible to measurements. The distance decay of electron tunneling has attracted significant attention of the theoretical^{129–131} communities in recent decades. Although the importance of specific pathways in the polypeptide structure vs the generic tunneling decay specified by the height of the potential barrier is still actively discussed,^{132–135} there is a general consensus about the magnitudes of matrix elements involved and the distance decay of the tunneling probability.^{132,136}

The last component of the biological electron-transfer picture, the reorganization energy, is probably least understood. Although the reorganization energy is the hallmark of the classical Marcus theory of electron transfer,⁵³ not much is known about both its value and the microscopic modes responsible for reorganization in protein¹³² and DNA¹³⁷ electron transfer. For proteins, the experimental evidence mostly comes from kinetic measurements of ruthenium-modified proteins introduced into the field by Gray and co-workers,¹³⁸ and some recent reports from computer simulations.^{93,139,140} Notice that computer simulations reported in the past were mostly limited to either very short trajectories^{66,82,139} or estimates of the reorganization energy from the Stokes shift,^{93,140} which does not necessarily provide the correct value of the reorganization energy defined through the variance of the energy gap.¹⁰⁴ The uncertainties of reorganization energy values have led Dutton and co-workers to suggest¹³³ a generic value of 0.7 eV for electronic transitions between cofactors not exposed to water with the provision that smaller values might be required for photosynthetic electron transfer. The fits of the photosynthetic rates have been attempted many times and extremely low values of the reorganization

energies (as low as 0.1 eV^{12,121}), completely unthinkable in light of our present simulations, have been reported in the literature.

Our present work gives a different perspective to the problem of the activation barrier of electron transfer in proteins. We claim that the range of reorganization energies fundamentally attainable in protein electron transfer is very broad given that the overall reorganization energy attained in our present and previous¹⁰⁴ simulations is much higher than it was previously anticipated (≈ 1.6 eV for the S1 protocol and ≈ 2.5 eV for the S2 protocol). The question of assigning the reorganization energy thus turns not into its “generic” value but into the question of finding the protein/solvent reorganization energy reachable on a given time scale of the reaction, when a certain portion of nuclear degrees of freedom is dynamically frozen.

We could not identify any specific solvent and/or protein modes that drive electron transfer. Instead, the energetics of electronic transitions appear to be driven by some generic set of ballistic modes which would probably characterize any heterogeneous solvent made of a rigid core (protein) surrounded by a molecular polar solvent (water). It also seems true that achieving both the reaction rate of primary charge separation and its low temperature dependence allows some, although not large, flexibility in the driving force (≈ 0.3 eV between photosynthetic bacteria¹²). Where the specific design of the reaction center appears to matter is in providing a sufficient tunneling rate between closely separated cofactors. This part of the design turns out to be very essential, since the fast rate allows the natural photosynthesis to dynamically freeze nuclear solvation, and to achieve low values of the reorganization parameters characterized by weak temperature dependence (ballistic motions and local density fluctuations). It might therefore turn out that “Darwin at the molecular scale”¹³³ operates not that much with redox potentials but, to a greater extent, with relaxation time scales.

Acknowledgment. This work was supported by the NSF (CHE-0616646) and by the DOE, Chemical Sciences Division, Office of Basic Energy Sciences (DEFG0207ER15908). CPU time was provided by ASU's Center for High Performance Computing. We are grateful to Prof. M. Marchi for sharing with us the force-field parameters of bacteriochlorophylls developed in his group. We also thank Prof. Mark Ratner for inspiring discussions of our results.

Appendix A: Simulation Protocol

Amber 8.0⁴⁷ was used for all MD simulations and minimizations. The initial configuration of the reaction center complex was taken from a crystal structure of the purple bacterium *Rhodobacter sphaeroides*.⁴² The force fields of bacteriochlorophylls, pheophytins, ubiquinones, and iron center were taken from Marchi and co-workers.⁸⁷ The protocol for the creation of solvated micelle was taken from ref 48 with the slight variations described below.

First, it should be mentioned that the reaction center was built without the carotenoid cofactor, since it was deemed unnecessary for the photosynthesis function.¹²⁴ The system was initially set up by protonating all lone valences and assuming standard pK_a values at pH 7. Next, conjugate gradient minimization was applied for $3N$ steps to remove bad contacts introduced by protonation (N is the total number of protein atoms). A detergent micelle was then created. The micelle was made by placing on a circle of eight LDAO molecules in the first quadrant at the $z = 0$ plane, with the heads pointing to the exterior and the tails pointing to the origin. Symmetry transformations were applied

about x and y axes to make a ring of 32 LDAO out of the first quadrant LDAO molecules. The ring was then copied and translated along the z -axis to create four more rings, each 7 Å apart. The protein was then rotated to align the quasi- C_2 axis with the z -axis, and translated so that the origin overlapped with the protein's center of mass. The rings were placed around the protein, making a tight fit, which covered almost the entire α helix region.

To help to form a micelle, the protein was allowed to relax by conjugate gradient minimization for another $3N$ steps while the LDAO were kept in place using a harmonic positional restraining force of 200 kcal/(mol Å²). Then, the force was removed and the system was slowly heated in a vacuum at a rate of 20 K/ps until 200 K. After this short time, the LDAO shell melted and collapsed into a tight micellar structure around the reaction center complex. The total energy of the system, the sum of the van der Waals and electrostatic energy, decreased during heating by several thousand kcal/mol, indicating the creation of a more stable structure. This step was different from Ceccarelli and Marchi's approach⁴⁸ which required heating to 400 K for several hundred ps in order to form a compact, equilibrated micelle. Once the micelle was formed, the system charge was neutralized with six sodium ions, while another 30 NaCl pairs were added to keep the system at an approximate 0.15 M salt concentration. Then, a total of 10 506 waters (10 503 in the charge-separated state) were added to form a truncated octahedron of the simulation cell.

Following the addition of the solvent and counterions, each system was run through an additional equilibration procedure. First, water was allowed to relax along a conjugate gradient minimization for $3N$ steps, while the micellar protein was held fixed with a weaker restraining force of 10 kcal/Å². Next, the full solvated micellar system was allowed to relax for another $3N$ steps to remove any remaining bad contacts. Following this minimization, the solvated system was heated again from 0 K to the desired temperature for 30 ps (NVT ensemble). After temperature equilibration, the volume was allowed to expand in a 2 ns NPT run, which stabilized in less than 200 ps. Once the density was equilibrated, NPT production runs lasting 5–15 ns (1–5 ns at $T = 77$ K) were used to calculate the averages.

A single 2 fs time step for all MD simulations was employed, SHAKE¹⁴¹ was used to constrain covalent bonds to hydrogen atoms, and the configurations were saved every 20 fs. For constant temperature and pressure, the system was coupled to a Berendsen thermostat and barostat, respectively. The long-range electrostatic interactions were handled using a smooth particle mesh Ewald summation with a 10 Å limit in the direct space sum.¹⁴²

Appendix B: Atomic Charges and Charge Transfer within the Special Pair

The partial charges of the electron-transfer cofactors are not provided by the Amber force field and need to be taken from quantum calculations. Due to the large size of the molecules, we modified the bacteriochlorophyll (Bchl) cofactors by replacing their phytyl side chains with methyl groups. The quantum calculations of these modified molecules were performed using GAMESS(US)¹⁴³ (B3LYP DFT/3–21G) and converted to partial charges by the CHELPG protocol, also implemented in GAMESS. The charge distribution of atoms of the phytyl chain was assumed to be the same for the neutral and charged cofactors and was calculated using the Antechamber module from Amber which employs the empirical AM1-BCC method. The full set of atomic charges (with phytyl chains) given in

Supporting Information Table S2 was used in the MD simulations. Similarly, the distribution of charge in the final charge-transfer state was obtained from DFT partial charges of a negatively charged Bchl[−] anion radical and a positively charged cation radical Bchl⁺ (Supporting Information Table S2). The positive charge was distributed unequally between the two Bchl's of the special pair, with $2/3$ of the positive charge residing on the L subunit (P_L) and $1/3$ of the positive charge residing on the M subunit (P_M), as suggested by ENDOR studies of *Rhodobacter sphaeroides*.¹⁴⁴ The set of Δq_k charges (k runs over the atoms of the cofactors) obtained by subtracting the atomic charges in the initial neutral state from the ionized state were used to calculate the Coulomb part of the donor–acceptor energy gap. The partial charges on the protein atoms were taken from the Amber FF03 force field,¹⁴⁵ and the TIP3P force field¹⁴⁶ was used for the partial charges of water.

We used Stark spectroscopy data by Lockhart and Boxer⁷⁰ as the starting point for determining the parameters of the charge-transfer state of the photoexcited special pair. The change in the absorption dipole moment within the special pair is about $f_c \Delta\mu = 7$ D larger than in an isolated bacteriochlorophyll, where $f_c \approx 1.2$ is the cavity field correction factor. If this change of the dipole moment difference, measured at 77 K, is connected to the mixing between the covalent ($P_M - P_L$)* and charge-separated, ($P_M^+ - P_L^-$)* states of the excited special pair, then this change in the dipole moment can be written as

$$\Delta\mu = n_{CT} \Delta\mu_{CT} \quad (B1)$$

where $\Delta\mu_{CT}$ is the dipole moment of the fully ionized state ($P_M^+ - P_L^-$)* and n_{CT} is the population of this state at the given energy gap between the neutral and ionized states. In terms of the two-state Hamiltonian, this population is given as

$$n_{CT} = \frac{1}{2} - \frac{\Delta\epsilon}{2\Delta\omega_p} \quad (B2)$$

where $\Delta\epsilon$ is the difference between diabatic energies of the neutral and ionized states (eq 37) and $\Delta\omega_p$ is the adiabatic energy gap between the eigenvalues of the two-state Hamiltonian

$$\Delta\omega_p = (\Delta\epsilon^2 + 4J^2)^{1/2} \quad (B3)$$

Here, J is the electronic coupling element between the neutral and ionized states of the excited special pair and, following Lathrop and Friesner,³⁵ we assume that the charge-transfer state ($P_M^+ - P_L^-$)* is predominantly mixed with the lower excitonic state of the dimer.

When two bacteriochlorophyll radicals, P_L^- and P_M^+ , are placed at their crystallographic positions, the resulting dipole moment of the fully ionized state is $\Delta\mu_{CT} = 40.2$ D. This implies that average charge mixing between the two states at 77 K is $n_{CT}(77 \text{ K}) = 0.143$. In order to determine the coupling parameter J from this number, we used the model vibronic Hamiltonian of Friesner and co-workers which was shown to reproduce a number of experimental properties (absorption, circular dichroism, polarized absorption).³⁵ In this model, the difference of energies between the ionized charge-transfer and neutral states of the special pair is 2800 cm^{−1}, which, combined with the population of charge-transfer state, gives $J = 979$ cm^{−1} and $\Delta\epsilon = 1998$ cm^{−1}. The former value falls in between 600 cm^{−1} used by Lathrop and Friesner³⁵ and 1450 cm^{−1} used by Renger.⁷⁸

The electronic mixing between the neutral and ionized states of the special pair will make its excited state more polarizable than the ground state. The change in the polarizability associated with charge transfer can be readily calculated from the two-state polarizability model which gives

$$\Delta\alpha = 2\Delta\mu_{\text{CT}}^2 J^2 / (\Delta\epsilon)^3 \quad (\text{B4})$$

With the parameters calculated above, this equation gives $\Delta\alpha = 707 \text{ \AA}^3$, consistent with $\Delta\alpha = 460\text{--}745 \text{ \AA}^3$ reported from fitting the Stark spectra.³⁸

The energy gap $\Delta\epsilon$ was obtained by fitting the spectra at 77 K³⁵ and is not directly suitable for our simulations at higher temperatures. The average energy gap between neutral and ionized states is made by the gas-phase gap $\Delta\epsilon^{\text{gas}}$ and a shift by polar and induction interactions with the protein/water solvent (eq 37). In order to extract this shift, we have run a short (1 ns) MD simulation of the reaction center at 77 K from which the solvent shift was determined to be -0.974 eV . This number allowed us to determine the gas-phase gap of $\Delta\epsilon^{\text{gas}} = 1.222 \text{ eV}$ which was used in the simulations of the polarizable special pair. The simulations required modification of the Sander module of AMBER such that the instantaneous energy gap and special pair charges are recalculated at each fifth time step of the MD run.

Appendix C: Fitting Experimental Kinetic Data

Our model was applied to two sets of experimental kinetic data, the temperature dependence of the primary rate from Fleming et al.¹ and time-resolved decays of the population of the photoexcited special pair from Wang et al.⁴³ For the latter set of data, recorded at $T = 300 \text{ K}$, we used the solvent reorganization energy from our MD simulations with the nonergodic correction extracted from the Stokes shift dynamics (eq 27). Population decays were calculated by self-consistently solving the diffusion-reaction Fokker–Planck equations (eqs 48–52) for the mutants used in the experiment (Supporting Information Table S1). In contrast to Wang et al.⁴³ who used three fitting parameters in their analysis, the reorganization energy is fixed here by MD simulations and only the gas-phase energy gap ΔE^{gas} and the electron-transfer matrix element V were varied to fit the rate constant at 300 K for mutant L170ND, which is very close to the wild-type reaction center with the difference between their midpoint potentials of only -0.007 eV .⁴³ This fit has resulted in $\Delta E^{\text{gas}} = 1.86 \text{ eV}$ and $V = 41.5 \text{ cm}^{-1}$ ($>60 \text{ cm}^{-1}$ was identified for this parameter in ref 147 and the value of 35 cm^{-1} was reported by Zhang and Friesner in ref 7).

Special pair mutants introduce electrostatic perturbations at the location of two sandwiched bacteriochlorophylls without significantly affecting the solvation component of the reaction Gibbs energy. This implies the variation of the inhomogeneous Coulomb component of the energy gap, $\Delta E_{\text{inh}}^{\text{C}}$. This component was varied in fitting the experimental $P(t)$ curves of other mutants while keeping the gas-phase gap and the electron-transfer matrix element constant. The variation of $\Delta E_{\text{inh}}^{\text{C}}$ with mutation relative to the wild-type reaction center then closely follows changes in the midpoint potential (Figure 17).

The gas-phase shift ΔE^{gas} and the matrix element V , obtained from fitting the rate at 300 K, were then used to calculate the temperature dependence of the rate. This calculation is complicated by the fact that all solvation energies and solvation relaxation times depend on temperature. The MD simulations do not provide sufficient accuracy to reliably estimate the temperature change of the Coulomb part of the reorganization parameters. Their temperature dependence was estimated from linear interpolations with the slopes listed in Table 4 (see also the discussion in section III.D). The temperature dependence of the induction component of the average gap is the main ingredient in reproducing the slope of the rate correctly. This

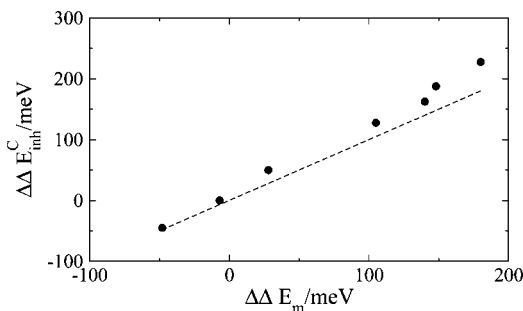


Figure 17. Correlation between the change of the inhomogeneous Coulomb energy gap $\Delta\Delta E_{\text{inh}}^{\text{C}}$ between mutants and wild-type reaction center and the corresponding changes in the midpoint redox potential $\Delta\Delta E_{\text{m}}$ reported experimentally.⁴³ The values of $\Delta\Delta E_{\text{inh}}^{\text{C}}$ are obtained from fitting the theoretical curves for the population decay to experiment⁴³ (Figure 12) while keeping the electron-transfer matrix element and the gas-phase gap constant. The data shown in the plot are also listed in Supporting Information Table S1. The dashed line indicates the unitary slope to guide the eye.

component is converged exceptionally well in MD simulations which were used to produce $\Delta E^{\text{ind}}(T)$.

The temperature dependence of the Stokes shift relaxation time makes the nonergodicity correction factor $f^{\lambda}(k_{\text{ET}})$ temperature-dependent as well. It turned out that only the relaxation time $\tau_2(T)$ is strongly temperature-dependent in the Stokes shift correlation function approximated by three components according to eq 21. The first two components were given constant values, $\tau_{\text{G}} = 0.1 \text{ ps}$ and $\tau_1 = 2.5 \text{ ps}$, and the longest relaxation time was given the Arrhenius temperature law $\ln \tau_2(T) = 0.936 + E_{\text{r}}/T$ with $E_{\text{r}} = 1212.3 \text{ K}$. The results of these calculations, shown in Figure 14, are in good agreement with the data by Fleming et al.¹ in the range of temperatures available to our simulations.

Supporting Information Available: Atomic charges of the bacteriochlorophyll cofactors from DFT calculations and Figures S1–S4. This material is available free of charge via the Internet at <http://pubs.acs.org>.

References and Notes

- (1) Fleming, G. R.; Martin, J. L.; Breton, J. *Nature* **1988**, *333*, 190.
- (2) Hoff, A. J.; Deisenhofer, J. *Phys. Rep.* **1997**, *287*, 1.
- (3) Page, C. C.; Moser, C. C.; Chen, X. X.; Dutton, P. L. *Nature* **1999**, *402*, 47.
- (4) Warshel, A.; Parson, W. W. *Q. Rev. Biophys.* **2001**, *34*, 563.
- (5) Blankenship, R. E. *Molecular Mechanisms of Photosynthesis*; Blackwell Science: Williston, VT, 2003.
- (6) Page, C. C.; Moser, C. C.; Dutton, P. L. *Curr. Opin. Biol.* **2003**, *7*, 551.
- (7) Zhang, L. Y.; Friesner, R. A. *Proc. Natl. Acad. Sci. U.S.A.* **1998**, *95*, 13603.
- (8) Ivashin, N.; Kallebring, B.; Larsson, S.; Hansson, O. *J. Phys. Chem. B* **1998**, *102*, 5017–5022.
- (9) Nishioka, H.; Kimura, A.; Yamato, T.; Kawatsu, T.; Kakitani, T. *J. Phys. Chem. B* **2005**, *109*, 1978–1987.
- (10) Bixon, M.; Jortner, J.; Mechel-Beyerle, M. E. *Chem. Phys.* **1995**, *197*, 389.
- (11) Bixon, M.; Jortner, J. *Adv. Chem. Phys.* **1999**, *106*, 35.
- (12) Volk, M.; Aumeier, G.; Langenbacher, T.; Feick, R.; Ogrodnik, A.; Michel-Beyerle, M.-E. *J. Phys. Chem. B* **1998**, *102*, 735.
- (13) de Winter, A.; Boxer, S. G. *J. Phys. Chem. A* **2003**, *107*, 3341–3350.
- (14) Noy, D.; Moser, C. C.; Dutton, P. L. *Biochim. Biophys. Acta* **2006**, *1757*, 90–105.
- (15) Rossky, P. J.; Simon, J. D. *Science* **1994**, *370*, 263.
- (16) Jimenez, R.; Fleming, G. R.; Kumar, P. V.; Maroncelli, M. *Nature* **1994**, *369*, 471.
- (17) Reynolds, L.; Gardecki, J. A.; Frankland, S. J. V.; Maroncelli, M. *J. Phys. Chem.* **1996**, *100*, 10337.

- (18) Maroncelli, M.; Fleming, G. R. *J. Chem. Phys.* **1988**, *89*, 5044–5069.
- (19) Fleming, G. R.; Wolyne, P. G. *Phys. Today* **1990**, *43*, 36–43.
- (20) Fenimore, P. W.; Frauenfelder, H.; McMahon, B. H.; Young, R. D. *Proc. Natl. Acad. Sci. U.S.A.* **2004**, *101*, 14408–14413.
- (21) Ediger, M. D.; Angell, C. A.; Nagel, S. R. *J. Phys. Chem.* **1996**, *100*, 13200.
- (22) Bagchi, B.; Chandra, A. *Adv. Chem. Phys.* **1991**, *80*, 1.
- (23) Richert, R. *J. Chem. Phys.* **2000**, *113*, 8404.
- (24) Ngai, K. L. *J. Non-Cryst. Solids* **2000**, *275*, 7.
- (25) Yang, Y.; Lai, W.-C.; Hsu, S. L. *J. Chem. Phys.* **2007**, *127*, 054901.
- (26) Ngai, K. L.; Capaccioli, S. *J. Phys.: Condens. Matter* **2007**, *19*, 205114.
- (27) Marchi, M.; Gehlen, J. N.; Chandler, D.; Newton, M. *J. Am. Chem. Soc.* **1993**, *115*, 4178.
- (28) Schmidt, S.; Arlt, T.; Hamm, P.; Huber, H.; Nägele, T.; Wachtveitl, J.; Meyer, M.; Scheer, H.; Zinth, W. *Chem. Phys. Lett.* **1994**, *223*, 116–120.
- (29) Ogorodnik, A.; Keupp, W.; Volk, M.; Aumeier, G.; Michel-Beyerle, M. E. *J. Phys. Chem.* **1994**, *98*, 3432–3439.
- (30) Holzwarth, A.; Muller, M. *Biochemistry* **1996**, *35*, 11820–11831.
- (31) Yakovlev, A. G.; Shkuropatov, A. C.; Shuvalov, V. A. *FEBS Lett.* **2000**, *466*, 209–212.
- (32) Zinth, W.; Wachtveitl, J. *ChemPhysChem* **2005**, *6*, 871–880.
- (33) Roberts, J.; Holten, D.; Kirmaier, C. *J. Phys. Chem. B* **2001**, *105*, 5575–5584.
- (34) Warshel, A. *Proc. Natl. Acad. Sci. U.S.A.* **1980**, *77*, 3105–3109.
- (35) Lathrop, E. J. P.; Friesner, R. A. *J. Phys. Chem.* **1994**, *98*, 3056–3066.
- (36) Reimers, J. R.; Shapley, W. A.; Hush, N. S. *J. Chem. Phys.* **2003**, *119*, 3240–3248.
- (37) van Amerongen, H.; Valkunas, L.; van Grondelle, R. *Photosynthetic Excitons*; World Scientific: Singapore, 2000.
- (38) Middendorf, T. R.; Mazzola, L. T.; Lao, K. Q.; Steffen, M. A.; Boxer, S. G. *Biochim. Biophys. Acta* **1993**, *1143*, 223.
- (39) Matyushov, D. V.; Voth, G. A. *J. Phys. Chem. A* **1999**, *103*, 10981.
- (40) Small, D. W.; Matyushov, D. V.; Voth, G. A. *J. Am. Chem. Soc.* **2003**, *125*, 7470.
- (41) Matyushov, D. V. *J. Phys. Chem. B* **2006**, *110*, 10095.
- (42) Ermler, U.; Fritzsche, G.; Buchanan, S. K.; Michel, H. *Structure* **1994**, *2*, 925–936.
- (43) Wang, H.; Lin, S.; Allen, J. P.; Williams, J. C.; Blankert, S.; Laser, C.; Woodbury, N. W. *Science* **2007**, *316*, 747.
- (44) Sumi, H.; Marcus, R. A. *J. Chem. Phys.* **1986**, *84*, 4894.
- (45) Nadler, W.; Marcus, R. A. *J. Chem. Phys.* **1987**, *86*, 3906–3924.
- (46) Zhu, J. J.; Rasaiah, J. C. *J. Chem. Phys.* **1991**, *95*, 3325.
- (47) Case, D. A.; Cheatham, T. E.; Darden, T.; Gohlke, H.; Luo, R.; Merz, K. M.; Onufriev, A.; Simmerling, C.; Wang, B.; Woods, R. J. *J. Comput. Chem.* **2005**, *26*, 1668–1688.
- (48) Ceccarelli, M.; Marchi, M. *J. Phys. Chem. B* **2003**, *107*, 1423.
- (49) Ceccarelli, M.; Marchi, M. *J. Phys. Chem. B* **2003**, *107*, 5630.
- (50) Kirmaier, G.; Laible, P. D.; Hindin, E.; Hanson, D. K.; Holten, D. *Chem. Phys.* **2003**, *294*, 305–318.
- (51) Matyushov, D. V. *Acc. Chem. Res.* **2007**, *40*, 294–301.
- (52) Kuharski, R. A.; Bader, J. S.; Chandler, D.; Sprik, M.; Klein, M. L.; Impey, R. W. *J. Chem. Phys.* **1988**, *89*, 3248.
- (53) Marcus, R. A.; Sutin, N. *Biochim. Biophys. Acta* **1985**, *811*, 265.
- (54) Pekar, S. I. *JETPh* **1946**, *16*, 341.
- (55) Pekar, S. I. *Research in electron theory of crystals*; USAEC: Washington, DC, 1963.
- (56) Frölich, H. *Adv. Phys.* **1954**, *3*, 325.
- (57) Feynman, R. P. *Phys. Rev.* **1955**, *97*, 660.
- (58) Matyushov, D. V.; Schmid, R. *J. Chem. Phys.* **1995**, *103*, 2034.
- (59) Matyushov, D. V. *J. Chem. Phys.* **2005**, *122*, 084507.
- (60) Marcus, R. A. *J. Chem. Phys.* **1956**, *24*, 966.
- (61) Raineri, F. O.; Friedman, H. L. *Adv. Chem. Phys.* **1999**, *107*, 81.
- (62) Kornyshev, A. A.; Sutmann, G. *J. Chem. Phys.* **1996**, *104*, 1524.
- (63) Milischuk, A. A.; Matyushov, D. V.; Newton, M. D. *Chem. Phys.* **2006**, *324*, 172–194.
- (64) Landau, L. D.; Lifshits, E. M. *Statistical Physics*; Pergamon Press: New York, 1980.
- (65) Ovchinnikov, A. A.; Ovchinnikova, M. Y. *JETPh* **1969**, *29*, 688.
- (66) Parson, W. W.; Chu, Z. T.; Warshel, A. *Biophys. J.* **1998**, *74*, 182.
- (67) Medvedev, E.; Kotelnikov, A.; Barinov, A.; Psikha, B.; Ortega, J.; Popovic, D.; Stuchebrukhov, A. *J. Phys. Chem. B* **2008**, *112*, 3208–3216.
- (68) Palmer, R. G. *Adv. Phys.* **1982**, *31*, 669–735.
- (69) Ghorai, P. K.; Matyushov, D. V. *J. Chem. Phys.* **2006**, *124*, 144510.
- (70) Lockhart, D. J.; Boxer, S. G. *Proc. Natl. Acad. Sci. U.S.A.* **1988**, *85*, 107–111.
- (71) Haran, G.; Wynne, K.; Moser, C. C.; Dutton, P. L.; Hochstrasser, R. M. *J. Phys. Chem.* **1996**, *100*, 5562–5569.
- (72) Wynne, K.; Haran, G.; Reid, G. D.; Moser, C. C.; Dutton, P. L.; Hochstrasser, R. M. *J. Phys. Chem.* **1996**, *100*, 5140–5148.
- (73) Arnett, D. C.; Moser, C. C.; Dutton, P. L.; Scherer, N. F. *J. Phys. Chem. B* **1999**, *103*, 2014–2032.
- (74) Larsson, S.; Kallbring, B. *Int. J. Quant. Chem.: Quant. Biochem. Symp.* **1990**, *17*, 189–206.
- (75) Thompson, M. A.; Zerner, M. C.; Fajer, J. *J. Phys. Chem.* **1991**, *95*, 5693–5700.
- (76) Zhou, H.; Boxer, S. G. *J. Phys. Chem. B* **1997**, *101*, 5759–5766.
- (77) Chang, C. H.; Hayashi, M.; Liang, K. K.; Chang, R.; Lin, S. H. *J. Phys. Chem. B* **2001**, *105*, 1216.
- (78) Renger, T. *Phys. Rev. Lett.* **2004**, *93*, 188101.
- (79) Matyushov, D. V.; Newton, M. D. *J. Phys. Chem. A* **2001**, *105*, 8516.
- (80) Matyushov, D. V.; Voth, G. A. *J. Chem. Phys.* **2000**, *113*, 5413.
- (81) Warshel, A.; Chu, Z. T.; Parson, W. W. *Science* **1989**, *246*, 112.
- (82) Treutlein, H.; Schulten, K.; Brünger, A. T.; Karplus, M.; Deisenhofer, J.; Michel, H. *Proc. Natl. Acad. Sci. U.S.A.* **1992**, *89*, 75.
- (83) Gehlen, J. N.; Marchi, M.; Chandler, D. *Science* **1994**, *263*, 499.
- (84) Sterpone, F.; Ceccarelli, M.; Marchi, M. *J. Phys. Chem. B* **2003**, *107*, 11208–11215.
- (85) van Duijnen, P.; Swart, M. *J. Phys. Chem. A* **1998**, *102*, 2399–2407.
- (86) Caldwell, J. W.; Kollman, P. A. *J. Phys. Chem.* **1995**, *99*, 6208–6219.
- (87) Ceccarelli, M.; Procacci, P.; Marchi, M. *J. Comput. Chem.* **2003**, *24*, 129–142.
- (88) Åqvist, J.; Warshel, A. *Chem. Rev.* **1993**, *93*, 2523–2544.
- (89) Schmitt, U. W.; Voth, G. A. *J. Chem. Phys.* **1999**, *111*, 9361–9381.
- (90) Bialek-Bylka, G. E.; Jazurek, B.; Dedic, R.; Hala, J.; Skrzypczak, A. *Cell. Mol. Biol. Lett.* **2003**, *8*, 689–697.
- (91) Sasisanker, P.; Oleinikova, A.; Weingartner, H.; Ravindra, R.; Winter, R. *J. Phys. Chem. Chem. Phys.* **2004**, *6*, 1899–1905.
- (92) Haffa, A. L. M.; Lin, S.; Katilius, E.; Williams, J. C.; Taguchi, A. K. W.; Allen, J. P.; Woodbury, N. W. *J. Phys. Chem. B* **2002**, *106*, 7376.
- (93) Sulpizi, M.; Raugei, S.; VandeVondele, J.; Carloni, P.; Sprik, M. *J. Phys. Chem. B* **2007**, *111*, 3969–3976.
- (94) Newton, M. D. *Adv. Chem. Phys.* **1999**, *106*, 303.
- (95) Ghorai, P. K.; Matyushov, D. V. *J. Phys. Chem. A* **2006**, *110*, 8857.
- (96) Ghorai, P. K.; Matyushov, D. V. *J. Phys. Chem. B* **2006**, *110*, 1866.
- (97) Ferrand, M.; Dianoux, A. J.; Petry, W.; Zaccari, G. *Proc. Natl. Acad. Sci. U.S.A.* **1993**, *90*, 9668–9672.
- (98) Bizzarri, A. R. *J. Phys.: Condens. Matter* **2004**, *16*, R83.
- (99) Kirmaier, C.; Holten, D. In *Photosynthetic Bacterial Reaction Center: Structure and Dynamics*; Breton, J., Vermégio, A., Eds.; Plenum: New York, 1988; Vol. 149.
- (100) Huber, H.; Meyer, M.; Scheer, H.; Zinth, W.; Wachtveitl, J. *Photosynth. Res.* **1998**, *55*, 153–162.
- (101) Renger, T.; Trostmann, I.; Theiss, C.; Madjet, M.; Richter, M.; Paulsen, H.; Eichler, H.; Knorr, A.; Renger, G. *J. Phys. Chem. B* **2007**, *111*, 10487–10501.
- (102) Vos, M. H.; Martin, J.-L. *Biochim. Biophys. Acta* **1999**, *1411*, 1–20.
- (103) Trissl, H.-W.; Bernhardt, K.; Lapin, M. *Biochemistry* **2001**, *40*, 5290–5298.
- (104) LeBard, D. N.; Matyushov, D. V. *J. Phys. Chem. B* **2008**, *112*, 5218.
- (105) Kapko, V.; Matyushov, D. V. *J. Phys. Chem. B* **2006**, *110*, 13184.
- (106) Vos, M. H.; Lambry, J.; Robles, S. J.; Youvan, D. C.; Breton, J.; Martin, J. *Proc. Natl. Acad. Sci. U.S.A.* **1991**, *88*, 8885–8889.
- (107) Du, M.; Rosenthal, S. J.; Xie, X.; DiMaggio, T. J.; Schmidt, M.; Hanson, D. K.; Schiffer, M.; Norris, J. R.; Fleming, G. R. *Proc. Natl. Acad. Sci. U.S.A.* **1992**, *89*, 8517–8521.
- (108) Chaudhury, S.; Cherayil, B. J. *J. Chem. Phys.* **2007**, *127*, 145103.
- (109) Agmon, N.; Hopfield, J. J. *J. Chem. Phys.* **1983**, *78*, 6947–6959.
- (110) Gayathri, N.; Bagchi, B. *J. Phys. Chem.* **1996**, *100*, 3056–3062.
- (111) Okuyama, S.; Oxtoby, D. W. *J. Chem. Phys.* **1986**, *84*, 5830–5835.
- (112) Hynes, J. T. *J. Phys. Chem.* **1986**, *90*, 3701–3706.
- (113) Walker, G. C.; Åkesson, E.; Johnson, A. E.; Levinger, N. E.; Barbara, P. F. *J. Phys. Chem.* **1992**, *96*, 3728.
- (114) Abbyad, P.; Shi, X.; Childs, W.; McAnaney, T.; Cohen, B.; Boxer, S. *J. Phys. Chem. B* **2007**, *111*, 8269–8276.
- (115) Sahu, K.; Mondal, S. K.; Ghosh, S.; Roy, D.; Bhattacharyya, K. *J. Chem. Phys.* **2006**, *124*, 124909.
- (116) Li, T.; Hassanali, A.; Kao, Y.-T.; Zhong, D.; Singer, S. *J. Am. Chem. Soc.* **2007**, *129*, 3376–3382.

- (117) Markelz, A. G.; Knab, J. R.; Chen, J. Y.; He, Y. *Chem. Phys. Lett.* **2007**, *442*, 413–417.
- (118) LeBard, D. N.; Matyushov, D. V. *J. Chem. Phys.* **2008**, *128*, 155106.
- (119) Edens, G. J.; Gunner, M. R.; Xu, Q.; Mauzerall, D. *J. Am. Chem. Soc.* **2000**, *122*, 1479.
- (120) Gunner, M. R.; Dutton, P. L. *J. Am. Chem. Soc.* **1989**, *111*, 3400–3412.
- (121) Sumi, H.; Kakitani, T. *J. Phys. Chem. B* **2001**, *105*, 9603.
- (122) Both PHE and TYR also absorb at 280 nm, and in addition, exposure to water makes fluorescence decay faster (see: McCammon, J. A.; Wolynes, P. G.; Karplus, M. *Biochemistry* **1979**, *18*, 927.). Although there are 39 TRP residues used to calculate the TRP Stokes shift dynamics, an additional 27 TYR and 58 PHE residues also exist in the wild type, which might have contributed to a faster decay of the correlation function compared to the TRP-only function calculated from MD simulations.
- (123) Windsor, M. W.; Menzel, R. *Chem. Phys. Lett.* **1989**, *164*, 143–150.
- (124) Cherepy, N.; Shreve, A.; Moore, L.; Boxer, S.; Mathies, R. *J. Phys. Chem. B* **1997**, *101*, 3250–3260.
- (125) Warshel, A.; Parson, W. W. *J. Am. Chem. Soc.* **1987**, *109*, 6143–6152.
- (126) Gupta, S.; Matyushov, D. V. *J. Phys. Chem. A* **2004**, *108*, 2087.
- (127) Parson, W. W.; Warshel, A. *Chem. Phys.* **2004**, *296*, 201.
- (128) Parson, W. W.; Warshel, A. *J. Phys. Chem. B* **2004**, *108*, 10474.
- (129) Beratan, D. N.; Betts, J. N.; Onuchic, J. N. *J. Phys. Chem.* **1992**, *96*, 2852–2855.
- (130) Skourtis, S. S.; Balabin, I. A.; Kawatsu, T.; Beratan, D. N. *Proc. Natl. Acad. Sci. U.S.A.* **2005**, *102*, 3552–3557.
- (131) Stuchebrukhov, A. A. *Adv. Phys. Chem.* **2001**, *118*, 1.
- (132) Gray, H. B.; Winkler, J. R. *Proc. Natl. Acad. Sci. U.S.A.* **2005**, *102*, 3534.
- (133) Moser, C. C.; Page, C. C.; Dutton, P. L. *Philos. Trans. R. Soc. London, Ser. B* **2006**, *361*, 1295–1305.
- (134) Jasaitis, A.; Johansson, M. P.; Wilkström, M.; Vos, M. H.; Verhovsky, M. I. *Proc. Natl. Acad. Sci. U.S.A.* **2007**, *104*, 20811–20814.
- (135) Beratan, D. N.; Balabin, I. A. *Proc. Natl. Acad. Sci. U.S.A.* **2008**, *105*, 403–404.
- (136) Goldsmith, R. H.; Sinks, L. E.; Kelley, R. F.; Betzen, L. J.; Liu, W.; Weiss, E. A.; Ratner, M. A.; Wasielewski, M. R. *Proc. Natl. Acad. Sci. U.S.A.* **2005**, *102*, 3540–3545.
- (137) Lewis, F. D.; Letsinger, R. L.; Wasielewski, M. R. *Acc. Chem. Res.* **2001**, *34*, 159.
- (138) Skov, L.; Pascher, T.; Winkler, J.; Gray, H. *J. Am. Chem. Soc.* **1998**, *120*, 1102–1103.
- (139) Cascella, M.; Magistrato, A.; Tavernelli, I.; Carloni, P.; Rothlisberger, U. *Proc. Natl. Acad. Sci. U.S.A.* **2006**, *103*, 19641–19646.
- (140) Blumberger, J.; Klein, M. L. *J. Am. Chem. Soc.* **2006**, *128*, 13854.
- (141) Ryckaert, J.-P.; Ciccotti, G.; Berendsen, H. J. C. *J. Comput. Phys.* **1977**, *23*, 327–341.
- (142) Essmann, U.; Perera, L.; Berkowitz, M. L.; Darden, T.; Lee, H.; Pedersen, L. G. *J. Chem. Phys.* **1995**, *103*, 8577–8593.
- (143) Schmidt, M. W.; Baldrige, K.; Boatz, J. A.; Elbert, S. T.; Gordon, M. S.; Jensen, J. H.; Koseki, S.; Matsunaga, N.; Nguyen, K. A.; Su, S. J.; Windus, T. L.; Dupuis, M.; Montgomery, J. A. *J. Comput. Chem.* **1993**, *14*, 1347.
- (144) Johnson, E. T.; Müh, F.; Navedryk, E.; Williams, J. C.; Allen, J. P.; Lubitz, W.; Breton, J.; Parson, W. W. *J. Phys. Chem. B* **2002**, *106*, 11859–11869.
- (145) Duan, Y.; Wu, C.; Chowdhury, S.; Lee, M. C.; Xiong, G.; Zhang, W.; Yang, R.; Cieplak, P.; Luo, R.; Lee, T.; Caldwell, J.; Wang, J.; Kollman, P. *J. Comput. Chem.* **2003**, *24*, 1999–2012.
- (146) Jorgensen, W. L.; Chandrasekhar, J.; Madura, J. D.; Impey, R. W.; Klein, M. L. *J. Chem. Phys.* **1983**, *79*, 926–935.
- (147) Bixon, M.; Jortner, J.; Michel-Beyerle, M. E.; Ogrodnik, A. *Biochim. Biophys. Acta* **1989**, *977*, 273–286.

JP8016503